

# Glypicans shield the Wnt lipid moiety to enable signalling at a distance

<https://doi.org/10.1038/s41586-020-2498-z>

Received: 8 August 2019

Accepted: 23 April 2020

Published online: 22 July 2020

 Check for updates

Ian J. McGough<sup>1,3</sup>, Luca Vecchia<sup>2,3</sup>, Benjamin Bishop<sup>2</sup>, Tomas Malinauskas<sup>2</sup>, Karen Beckett<sup>1</sup>, Dhira Joshi<sup>1</sup>, Nicola O'Reilly<sup>1</sup>, Christian Siebold<sup>2</sup>, E. Yvonne Jones<sup>2,4</sup>✉ & Jean-Paul Vincent<sup>1</sup>✉

A relatively small number of proteins have been suggested to act as morphogens–signalling molecules that spread within tissues to organize tissue repair and the specification of cell fate during development. Among them are Wnt proteins, which carry a palmitoleate moiety that is essential for signalling activity<sup>1–3</sup>. How a hydrophobic lipoprotein can spread in the aqueous extracellular space is unknown. Several mechanisms, such as those involving lipoprotein particles, exosomes or a specific chaperone, have been proposed to overcome this so-called Wnt solubility problem<sup>4–6</sup>. Here we provide evidence against these models and show that the Wnt lipid is shielded by the core domain of a subclass of glypicans defined by the Dally-like protein (Dlp). Structural analysis shows that, in the presence of palmitoleoylated peptides, these glypicans change conformation to create a hydrophobic space. Thus, glypicans of the Dlp family protect the lipid of Wnt proteins from the aqueous environment and serve as a reservoir from which Wnt proteins can be handed over to signalling receptors.

Wnt proteins are lipidated<sup>1</sup>, with a palmitoleate<sup>2</sup> appended to a conserved serine residue (Ser209 in human WNT3A). Crystal structures have shown how the Wnt palmitoleate contributes directly to engagement with the Frizzled receptor and hence signalling activity<sup>3</sup>. Despite being lipidated, and therefore hydrophobic, Wnt proteins can act over several cell diameters, although the range may vary depending on the tissue. Long-range action has been suggested to organize the anterior–posterior axis of *Xenopus* embryos<sup>7</sup>, and juxtacrine action could suffice in the mouse intestinal crypt<sup>8</sup>. Flies relying solely on membrane-tethered Wingless (the main Wnt protein in *Drosophila*) are morphologically normal, but experience several phenotypes such as delayed development, sterility and reduced food intake<sup>9,10</sup>. Even in wing precursors, in which long-range action is not essential for patterning, Wingless spreads over more than ten cell diameters<sup>11</sup> and contributes to timely growth and full activation of target genes<sup>9</sup>. Because extracellular Wingless is readily detectable in wing imaginal discs, they constitute a good tissue in which to study its spread in a physiological setting.

## Models of Wnt transport

Previous work has suggested that lipoprotein particles (LPPs) or exosomes could transport Wnt in the extracellular space<sup>4,5</sup>. To test whether endogenously expressed Wingless interacts with these structures, we devised a trapping assay inspired by the morphotrap approach<sup>12</sup>. A membrane-tethered anti-GFP nanobody (Vhh4-CD8) was used to capture GFP–Wingless expressed from a knock-in allele. This led to the enrichment of GFP–Wingless at the surface of expressing cells (Extended Data Fig. 1a), but not of lipophorin, a component of LPPs, or the ESCRT protein Hrs, a marker of exosomes (Extended Data Fig. 1b, c). A secreted form of Dlp that is known to bind Wingless<sup>13,14</sup> and lacks the

glycophosphatidylinositol (GPI) membrane anchor (Dlp<sup>ΔGPI</sup>) was used as a positive control (Extended Data Fig. 1d–e). Moreover, we found that GFP–Wingless trapped by the NRT–Myc–LaG16 morphotrap (a LaG16 nanobody conjugated to the transmembrane protein neurotactin (NRT) with a Myc tag) had no effect on the distribution of haemagglutinin (HA)-tagged Wingless expressed from the other endogenous allele (Fig. 1a). This result argues against transport mechanisms involving several Wingless molecules such as exosomes, LPPs or micelles.

We next designed genetic tests to assess the possible roles of exosomes and LPPs further. Because there is no specific way to prevent the formation of exosomes, we inhibited the biogenesis of multivesicular bodies from where exosomes originate. This was achieved by expressing a dominant-negative form of VPS4 (VPS4<sup>DN</sup>) that is required for the final step in the invagination of luminal vesicles. Within 8 h of expression, ubiquitinated proteins accumulated, as expected, but there was no effect on the distribution of extracellular Wingless (Extended Data Fig. 2a). Similarly, the spread of Wingless appeared normal within tissues lacking Hrs, another ESCRT component (Extended Data Fig. 2b). To assess the role of LPPs, we modulated the activity of their receptors (Lpr1 and Lpr2) by gain- and loss-of-function manipulations. Overexpression of the Lpr2E isoform (for a period of 36 h) depleted available lipophorin from the extracellular space (Extended Data Fig. 2c) but did not affect levels of extracellular Wingless (Extended Data Fig. 2d). By contrast, deletion of both Lpr1 and Lpr2 also had no effect on extracellular or total Wingless, despite perturbing LPP uptake (Extended Data Fig. 2e).

An alternative model for Wnt transport involves Swim, a lipocalin that solubilizes Wingless in S2 cell culture medium<sup>6</sup>. To confirm an initial RNA interference (RNAi)-based assessment of the role of Swim (Extended Data Fig. 3a), we generated a genomic deletion that removes

<sup>1</sup>The Francis Crick Institute, London, UK. <sup>2</sup>Division of Structural Biology, Wellcome Centre for Human Genetics, University of Oxford, Oxford, UK. <sup>3</sup>The authors contributed equally: Ian J. McGough, Luca Vecchia. <sup>4</sup>These authors jointly supervised this work: E. Yvonne Jones, Jean-Paul Vincent. ✉e-mail: yvonne@strubi.ox.ac.uk; jp.vincent@crick.ac.uk

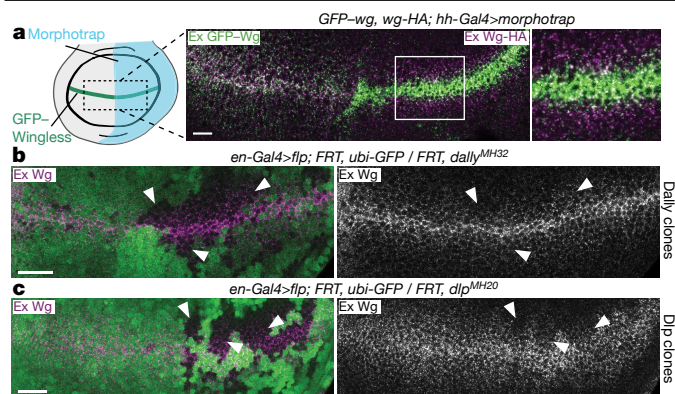


**Fig. 1 | Spread of Wingless does not involve multimeric assemblies but requires Dlp.** **a**, Morphotrap (NRT-Myc-LaG16) driven in the posterior compartment by *hh-Gal4* captures extracellular (Ex) GFP-Wingless (GFP-Wg), but not Wingless-HA (both expressed from knock-in alleles). In the control anterior compartment, both forms of Wingless show a graded distribution. The experiment was repeated independently three times with similar results. **b, c**, Extracellular Wingless is reduced to a greater extent in clones lacking Dlp than in clones lacking Dally (clones marked by the absence of GFP (white arrowheads)). Scale bars, 10  $\mu\text{m}$  (**a**) 25  $\mu\text{m}$  (**b, c**). The experiments were repeated independently three times with similar results.

the entire coding region (*Swim<sup>KO</sup>*) (Extended Data Fig. 3b). Homozygotes, lacking all gene function, were healthy and fertile with no apparent phenotype. Moreover, the distribution of total and extracellular Wingless was indistinguishable in *Swim<sup>KO</sup>* homozygotes and control wing imaginal discs (Extended Data Fig. 3c). No change in the Wingless target gene *Distal-less* was observed (Extended Data Fig. 3c). We conclude that Swim is entirely dispensable for Wingless transport, although we cannot exclude a possible redundant role, perhaps in combination with another lipocalin. In summary, our analysis so far has provided evidence against all the previously proposed mechanisms of Wnt transport, except for that involving cytonemes<sup>15</sup>, for which specific genetic tools are lacking. We therefore set out to re-investigate the role of glypicans, a class of proteins known to modulate the extracellular distribution of Wnt<sup>13,14</sup>.

### A subset of glypicans bind the Wnt lipid

Extensive genetic analysis has demonstrated the role of the *Drosophila* glypicans Dally and Dlp in ensuring proper extracellular distribution of Wingless<sup>13,14,16</sup>. Indeed, Wingless is markedly reduced at the surface of cells that lack both glypicans (Extended Data Fig. 3d). Mutations in *sulfateless*, which impair the addition of heparan sulfate chains on glypicans, also lead to a strong reduction in extracellular Wingless, and phenocopy the loss of Wingless signalling<sup>16</sup>. This is consistent with Wnt proteins binding heparan sulfate chains<sup>17</sup>, which decorate both Dlp and Dally. Notably, however, the loss of Dlp has a more marked effect on extracellular Wingless than the loss of Dally (Fig. 1b, c). Dlp binding to Wingless has been reported to involve two sites: one that involves the heparan sulfate chains, and the other involving the protein core<sup>13</sup>. We considered the possibility that the core site could mediate the interaction that shields the palmitoleate of Wnt.

We first asked to what extent Wingless needs to be lipidated to bind Dlp in vivo by comparing the ability of overexpressed Dlp to trap palmitoleoylated and non-palmitoleoylated Wingless at the surface of imaginal discs cells. Dlp overexpressed in a stripe that transects the normal stripe of *wingless* expression duly trapped endogenous-level GFP-Wingless (Fig. 2a). By contrast, Dlp did not detectably trap GFP-Wingless(S239A), even though this unlipidated form of Wingless is secreted<sup>14,18,19</sup> and trappable by Vhh4-CD8 (morphotrap)

(Extended Data Fig. 4a). We next assessed whether Dlp has standalone palmitoleate-binding activity by measuring its interaction with palmitoleoylated and control unlipidated peptide (both biotinylated). Catalytically dead Notum, which has a marked preference for the palmitoleoylated peptide<sup>20</sup>, served as a positive control. Dlp<sup>core</sup> (the minimal globular protein core lacking the GPI anchor and heparan sulfate chains) also bound preferentially to the palmitoleoylated peptide whereas Dally<sup>core</sup> had no such activity (Extended Data Fig. 4b). Prompted by these findings, we purified Dlp<sup>core</sup> and Dally<sup>core</sup> and investigated their binding properties by biolayer interferometry. Dlp<sup>core</sup> bound the palmitoleoylated version with sub-micromolar affinity (Fig. 2b, Extended Data Fig. 4c) but had no detectable affinity for the non-palmitoleoylated peptide (Extended Data Fig. 4d). Dally<sup>core</sup> showed no measurable interaction with palmitoleoylated peptide (Fig. 2b). We conclude that Dlp, but not Dally, has palmitoleate-binding activity.

Sequence conservation shows that the six human glypican proteins can be distinguished according to their homology to Dlp or Dally. We expressed two of each class in wing imaginal discs. Of these, human GPC4 and GPC6 (homologous to *Drosophila* Dlp) trapped Wingless, whereas human GPC3 and GPC5 (homologous to Dally) did not (Fig. 2, Extended Data Fig. 4e). Therefore, lipid binding activity seems to be a hallmark of the Dlp class of glypicans. Overexpressed Dlp has previously been shown to have biphasic activity in wing imaginal discs<sup>13,14</sup>, inhibiting the high target gene *senseless*, but extending the range of the low target gene *distal-less*. This could be explained if Dlp competed with Frizzled for lipid binding (decreasing signalling) while at the same time promoting long-range transport by shielding the Wingless lipid. Notably, human GPC4 and GPC6, but not GPC3 and GPC5, displayed a similarly biphasic activity (Extended Data Fig. 5a, b). Therefore, human glypicans of the Dlp family could modulate the extracellular behaviour of Wnt proteins through their palmitoleate-binding activity.

### Solubilization of Wingless by glypicans

Soluble Wnt cannot be recovered from serum-free medium conditioned by Wnt-expressing cells<sup>15,6,21</sup>. This is probably because of the absence of an activity that shields the palmitoleate. Indeed, the addition of lipid-binding proteins, such as Afamin or Swim, to the culture medium enables the release of soluble Wnt<sup>6,22</sup>. To confirm the lipid-binding activity of Dlp and mammalian Dlp orthologues, we tested whether they too could solubilize Wingless. S2 cells were induced to co-express secreted forms of glypicans (lacking their membrane anchor,  $\Delta\text{GPI}$ ) and GFP-Wingless in serum-free medium. Although Dlp <sup>$\Delta\text{GPI}$</sup>  enabled large amounts of GFP-Wingless to be recovered in the supernatant, Dally <sup>$\Delta\text{GPI}$</sup>  did not (Fig. 2d). A similar effect was seen after the addition of Dlp <sup>$\Delta\text{GPI}$</sup>  in the culture medium of GFP-Wingless-expressing cells (Extended Data Fig. 5c), showing that co-secretion is not needed for Dlp <sup>$\Delta\text{GPI}$</sup>  to solubilize Wingless. Similarly, secreted human GPC4 and GPC6 solubilized GFP-Wingless, whereas secreted human GPC3 and GPC5 did not (Fig. 2e). Solubilization enables signalling, as co-expression with Dlp was needed for transfected GFP-Wingless to activate a luciferase-based reporter (Extended Data Fig. 5d). Accordingly, an unidentified HSPG shown previously to stabilize Wnt activity<sup>21</sup> is probably a Dlp-class glypican. We conclude that glypicans of the Dlp family bind palmitoleate and thus contribute to the release of signalling-competent Wnt.

### Palmitoleate-bound conformation of Dlp

We set out to identify the molecular determinants of palmitoleate binding by the Dlp protein core. The crystal structure of Dlp<sup>core</sup> has previously been reported<sup>23</sup> and structural comparison has suggested that its N-terminal region is distantly related to the extracellular cysteine-rich domain (CRD) of the Frizzled family of Wnt receptors<sup>24</sup>. Given that the Frizzled CRD (Fzd<sup>CRD</sup>) provides a groove-like binding site for palmitoleate<sup>3</sup>, we first looked for the equivalent groove in the

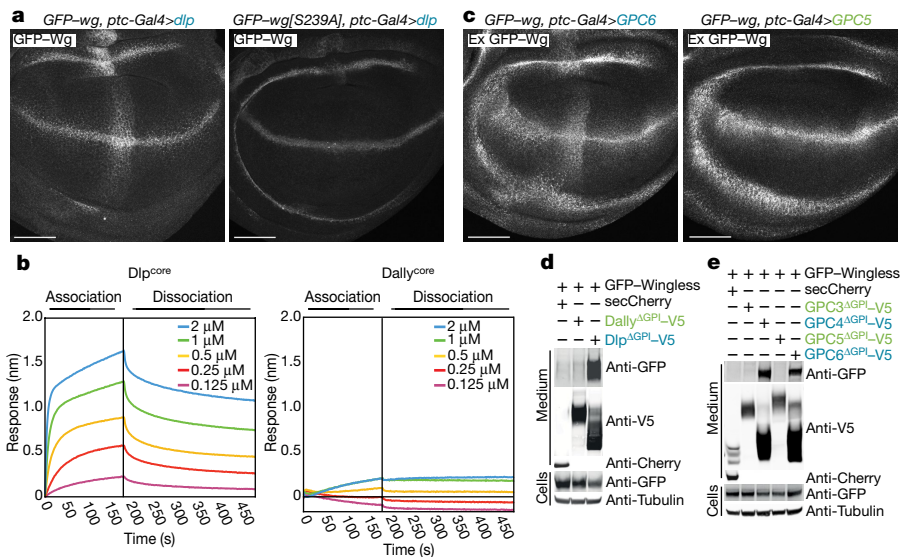


**Fig. 2 | A subset of glypicans bind palmitoleate. a**, Dlp driven by *ptc-Gal4* (transversal to the Wingless stripe) captures GFP–Wingless but not GFP–Wingless(S239A). The experiments were repeated independently three times with similar results. Scale bars, 50  $\mu\text{m}$ . **b**, Representative reference-subtracted biolayer interferometry traces of Dlp<sup>core</sup> and Dally<sup>core</sup> tested against biosensors loaded with palmitoleoylated peptides (sequence from human WNT7A, chosen because of improved solubility relative to the Wingless sequence). Only the Dlp<sup>core</sup>–palmitoleoylated peptide pair gave a signal. The experiments were repeated independently three times with similar results. **c**, Human GPC6 (Dlp family), but not human GPC5 (Dally family), expressed with *ptc-Gal4* captured

GFP–Wingless at the cell surface. Scale bars, 50  $\mu\text{m}$ . **d, e**, Members of the Dlp, but not Dally, family stabilize GFP–Wingless in solution. S2 cells, cultured in serum-free medium, were co-transfected with GFP–Wingless and non-membrane tethered ( $\Delta\text{GPI}$ ) V5-tagged forms of the indicated glypicans, or a secreted form of Cherry (negative control). Medium was collected and concentrated 20-fold and the amount of Wingless in solution was determined by western blot. These proteins could be sulfated, which may contribute to their solubilizing activity. Dlp family members run at lower sizes than predicted, perhaps because of processing by furin. The experiments were repeated independently three times with similar results.

uncomplexed (apo) structure of Dlp<sup>core</sup>. Superposition of the structure of apo Dlp<sup>core</sup> onto those of Fzd<sup>CRD</sup>–Wnt complexes<sup>3,25</sup> showed that, in Dlp, the CRD is more compact and the putative binding groove is shallower (Extended Data Fig. 6a–f). Notably, glypican CRDs contain an additional  $\alpha$ -helix that is located transversally to the entrance of the groove, thereby blocking lipid insertion (Extended Data Fig. 6g, h). This holds for structures of Dlp and human GPC1<sup>26</sup>.

The groove-blocking helix of the glypican CRD architecture renders an analogy with the palmitoleate-binding properties of the Frizzled CRDs untenable. We therefore sought to discover the site of palmitoleate-binding in Dlp<sup>core</sup> by direct experiment. The 2.21  $\text{\AA}$  resolution crystal structure for Dlp<sup>core</sup> in complex with a palmitoleoylated peptide was determined. The overall structure of uncomplexed Dlp<sup>core23</sup> is conserved in the complex, with a global main-chain root mean square deviation (r.m.s.d.) value of 1.98  $\text{\AA}$  (for 355 equivalent C $\alpha$  pairs) (Fig. 3a). Some additional portions of the Dlp<sup>core</sup> N-terminal segment were visible. These include an  $\alpha$ -helix, which we named  $\alpha\text{H0}$  (for helix nomenclature, see Extended Data Fig. 7a) and a 30-residue unstructured loop, similar to that seen in the published structure of human GPC1<sup>26</sup>. However, the region corresponding to the palmitoleate-binding groove of Fzd<sup>CRD</sup> remains occluded by the transversal  $\alpha$ -helix ( $\alpha\text{H1}$ ) (Extended Data Fig. 6g, h). Crucially, additional electron density, consistent with a palmitoleate acyl chain (Extended Data Fig. 8, Methods), was present on the opposite side of the Dlp<sup>core</sup>, in the so-called C-lobe<sup>23</sup>. Well-ordered electron density revealed the acyl chain, the ester bond with associated serine side chain and the serine main chain of the palmitoleoylated peptide. The remainder of the peptide lacks a well-defined conformation in the complexed structure. Most of the interactions between Dlp and the Wnt peptide are hydrophobic and involve the palmitoleate, consistent with our biophysical and biochemical data showing the interaction requires the lipid moiety.

Superposition of the apo and complexed Dlp<sup>core</sup> structures revealed that palmitoleate binding is associated with a conformational rearrangement in which helix  $\alpha\text{H9}$  and  $\alpha\text{H10}$  tilt away from the opposing

helix,  $\alpha\text{H1}$ , to generate a substantial shift in position (approximately 6  $\text{\AA}$  between apo and complexed structures at P365). An analysis of lattice contacts with neighbouring molecules indicated that the rearrangement was unlikely to result from the crystal environment (Methods). This movement opens a tunnel-like cavity to accommodate the palmitoleate (Fig. 3b). The cavity is lined with hydrophobic residues contributed by six C-lobe  $\alpha$ -helices (L164, L165 and F172 of  $\alpha\text{H1}$ ; F191, L194, F195 and L198 of  $\alpha\text{H2}$ ; F216 of  $\alpha\text{H3}$ ; L259, I263 and F267 of  $\alpha\text{H5}$ ; I359 and V363 of  $\alpha\text{H9}$  and L366 of  $\alpha\text{H10}$ ) (Fig. 3c). The 16-carbon (C16) acyl chain of the palmitoleate adopts an extended conformation resembling those reported for the Wnt-attached lipid in Fzd<sup>CRD</sup>–Wnt complexes<sup>3,25</sup>, but markedly different from that observed for lipid-binding to Notum<sup>20</sup>, which requires a kink in the palmitoleate (at the C9–C10 *cis* double bond). Notably, the palmitoleate only occupies the narrower, top part of the cavity generated by the conformational change in complexed Dlp<sup>core</sup>, leaving substantial space in the bottom part of the cavity (Extended Data Fig. 7b).

### Mutations impairing palmitoleate-binding

To functionally validate our structural findings, we designed Dlp mutants to interfere with Wnt binding (Fig. 3b, c). We initially aimed to hamper lipid insertion into the cavity either by introducing a bulky residue (S168M) at the entrance, or by engineering a disulfide bridge to prevent  $\alpha\text{H10}$  and  $\alpha\text{H1}$  from coming apart and hence locking Dlp in the closed, apo conformation (N367C on  $\alpha\text{H10}$  and M175C on  $\alpha\text{H1}$ ). As a first step, fluorescence-detection size exclusion chromatography (FSEC) was used to assess the binding of purified Dlp<sup>core</sup> variants to bodipy 505/512-labelled palmitic acid. Dlp<sup>core</sup> (as recognized by the 280-nm protein peak) co-eluted with bodipy fluorescence, indicating binding and hence some level of promiscuity in its lipid-binding activity. As expected, binding to bodipy–palmitate was substantially reduced for both mutant proteins (Fig. 4a). These proteins were also impaired in their ability to trap endogenous Wingless in vivo, albeit

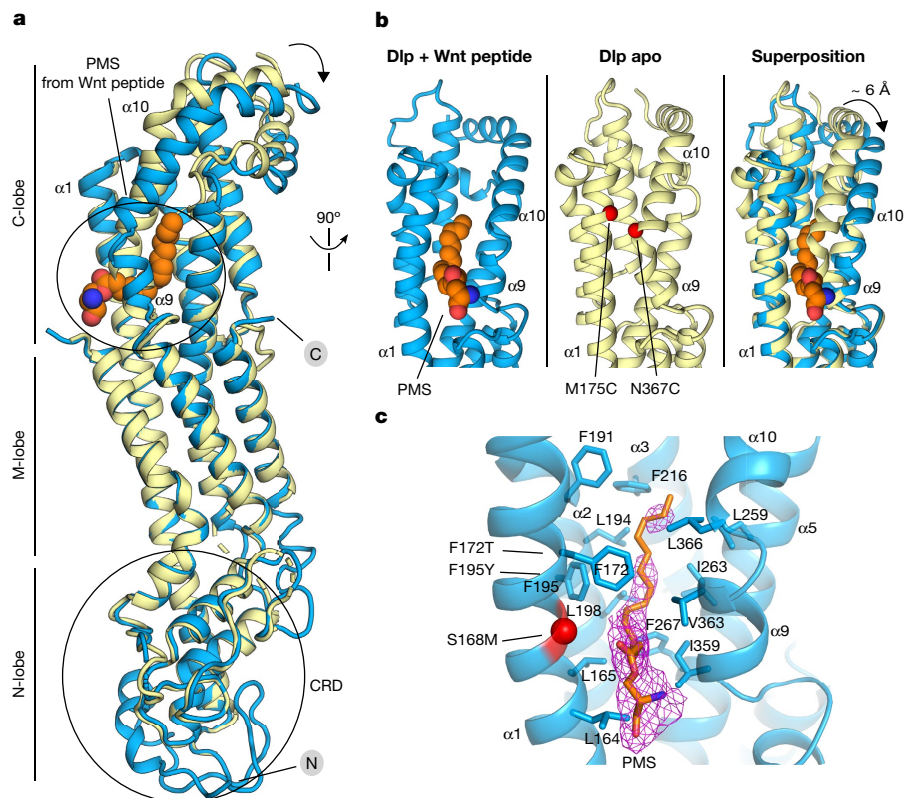


**Fig. 3 | Structural basis of glypican-Wnt peptide interaction.**

**a**, Superposition between the Dlp<sup>core</sup> apo structure (PDB code 3odn, pale yellow) and Dlp<sup>core</sup> in complex with human WNT7A palmitoleoylated peptide (marine). The palmitoleoylated serine (PMS) from WNT7A peptide is depicted in spheres in atomic colouring (C: orange, N: blue, O: red). N and C termini are indicated. The black arrow indicates domain movement of the C lobe between apo and palmitoleoylated Wnt7 peptide-bound form. **b**, Close-up view of the Dlp C-lobe, revealing the conformational rearrangement of helices  $\alpha 9$  and  $\alpha 10$  opening the Wnt-binding pocket. M175 and N367 of Dlp mutated to cysteine

residues to form a disulfide bridge to interfere with Wnt binding are indicated by red spheres. **c**, Close-up view of the lipid-binding pocket. Stick representation of residues lining the binding pocket (located within a 4.5 Å range from the Wnt peptide lipid for hydrophobic interactions). The red sphere indicates the site of one of the mutations predicted to interfere with Wnt binding (S168M). The positions of the F172T/F195Y mutations are also labelled. The  $F_o - F_c$  omit electron density map for the Wnt peptide palmitoleate is shown in purple chicken wire presentation, contoured at 2.5 $\sigma$ .

to different extents; of the two, only the N367C/M175C mutation completely abrogated in vivo trapping, whereas the Dlp(S168M)<sup>ΔGPI</sup> mutant retained some activity (Fig. 4b). Accordingly, Dlp(S168M)<sup>ΔGPI</sup> and Dlp(N367C/M175C)<sup>ΔGPI</sup> were less efficient than wild-type Dlp<sup>ΔGPI</sup> at solubilizing GFP-Wingless in culture medium (Fig. 4c). We further used the in vivo trapping assay to investigate the functional relevance of sequence differences between Dally and Dlp (Extended Data Fig. 9a). Mutations in Dlp to replace hydrophobic residues with polar ones (Dlp(F172T/F195Y)), or to introduce the putative glycosylation site of Dally (Dlp(R169E/T170N/Q171M/F172T)), reduced trapping, although not completely (Extended Data Fig. 9b). Dally mutations that remove the predicted glycosylation site and restore the hydrophobic Phe residue (Dally(E149R/N150T/M151Q/T152F)) did not confer lipid-binding activity. These results suggest that the difference in Wnt-binding activity between Dlp and Dally cannot be solely ascribed to residues at the entrance or within the tunnel. Because Dlp(N367C/M175C)<sup>ΔGPI</sup> had no in vivo trapping activity (Fig. 4b), even at the high level of expression achieved by the Gal4 system, we suggest that the movement of  $\alpha 10$  relative to  $\alpha 1$ , as observed in the crystal structure, is essential for tunnel formation and lipid binding.

## Discussion

On the basis of various lines of evidence against the possible roles of exosomes, lipoprotein particles and Swim in the spread of Wingless, we re-examined the binding of Wingless to glypicans. We found that—of the

two glypicans encoded by the *Drosophila* genome—Dlp, but not Dally, has palmitoleate-binding activity. This activity is conserved among human glypicans of the Dlp class and is not present among human homologues of Dally. We suggest that Dlp-class glypicans have evolved lipid-binding activity to shield the lipid of Wnt proteins, and possibly, that of other signalling molecules such as palmitate and/or cholesterol on Hedgehog family members. As we showed, the Dlp core (devoid of heparan sulfate chains) can sequester the palmitoleate moiety of Wnt peptides by forming a tunnel-like binding cavity. A combination of differences between Dlp and Dally, such as the nature of residues at the entrance and within the cavity, as well as structural features that allow  $\alpha 9$  and  $\alpha 10$  to shift relative to  $\alpha 1$ , could account for the lipid-binding activity of Dlp-class glypicans.

Glypicans of the Dlp class are not the only extracellular lipid-binding proteins. For example, *Drosophila* Frizzled3, a decoy receptor of Wingless<sup>27</sup> has been shown to hold signalling-competent Wingless at the cell surface<sup>28</sup>. In addition, secreted Frizzled related proteins are known to aid Wnt diffusion in vertebrates<sup>29</sup>. Thus, several extracellular proteins have the capacity to shield the palmitoleate of Wnt. We suggest nevertheless that several features of Dlp-class glypicans make them particularly suitable for Wnt transport along epithelia. Their GPI anchor facilitates rapid diffusion within the cell membrane while ensuring retention in the plane of the epithelium. Moreover, dual binding, through long heparan sulfate chains and the hydrophobic tunnel, could enable handover from one Dlp-class glypican to another, facilitating cell-to-cell transfer (Extended Data Fig. 9c). At some frequency, Wnt

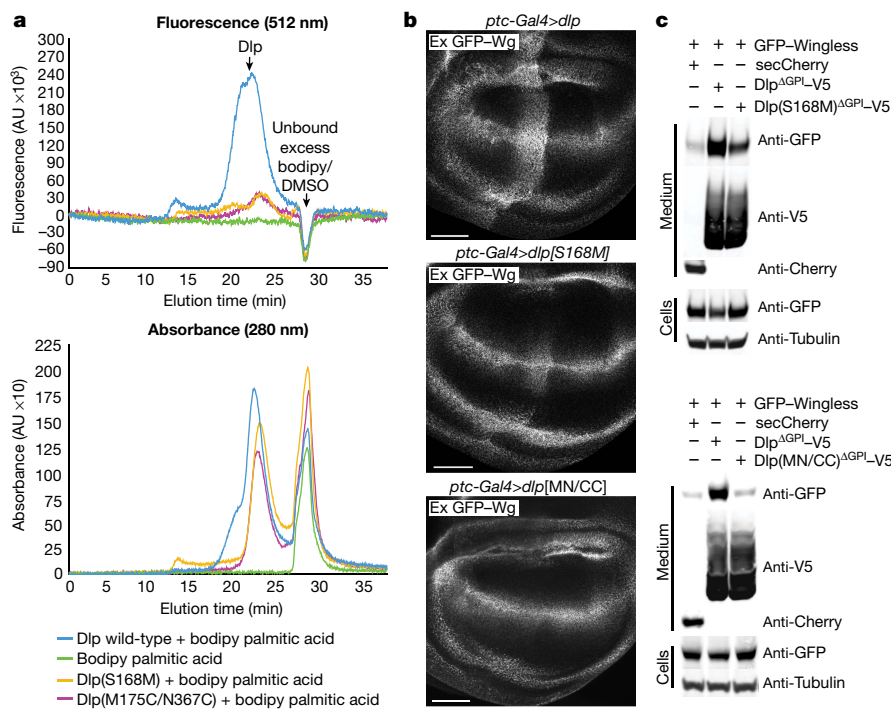


**Fig. 4 | Structure-guided point mutants impair Dlp lipid interaction.**

**a**, Representative FSEC profiles of purified wild-type Dlp<sup>core</sup> (blue) and the S168M (yellow), M175C/N367C (purple) mutants incubated with bodipy-labelled palmitic acid (C16:0), showing a reduction of fluorescence emission of mutants with respect to wild-type. This is suggestive of diminished binding affinity. The fluorophore profile in absence of proteins (green) is presented as control. The protein absorbance at 280 nm confirms protein presence, similar elution of wild-type and mutant proteins (ruling out mis-folding artefacts) and co-elution with the fluorescent peak. The experiments were repeated independently three times with similar results.

**b**, Dlp-HA, Dlp(S168M)-HA and Dlp(M175C/N367C)-HA were overexpressed with *ptc-gal4* and wing discs were stained for extracellular Wingless. Scale bars, 50  $\mu$ m. The experiments were repeated independently three times with similar results. **c**, Dlp(S168M)<sup>ΔGPI</sup> less efficiently stabilizes GFP-Wingless in solution than Dlp<sup>ΔGPI</sup>, whereas Dlp(M175C/N367C)<sup>ΔGPI</sup> has virtually no solubilization activity. S2 cells, cultured in serum-free medium, were co-transfected with GFP-Wingless and V5-tagged Dlp(S168M)<sup>ΔGPI</sup>, Dlp(M175C/N367C)<sup>ΔGPI</sup>, Dlp<sup>ΔGPI</sup> or a secreted Cherry. Medium was collected and concentrated 20-fold and the amount of wingless in solution determined via western blot. The experiments were repeated independently three times with similar results.

proteins would transfer from Dlp-class glypicans to Frizzled receptors to initiate signalosome assembly, as previously suggested (see figure 5d in ref. <sup>14</sup>). Although Dally is not essential for Wingless activity in *Drosophila*, it must contribute since the phenotype of *dally dlp* double mutants is stronger than that of the single *dlp* mutant (partial redundancy)<sup>13,14,30,31</sup>. It is likely that Dally-class glypicans bind Wnt proteins via their heparan sulfate chains. However, because they lack lipid-binding activity, the glypicans of this class would promptly off-load their cargo to a Frizzled receptor, thus serving only as co-receptors. Our results suggest that Dlp-class glypicans constitute an easily accessible reservoir of signalling-competent Wnt at the surface of signalling cells. In chick embryos, neural crest cells have been shown to carry and deliver Wnt proteins at a distance in a GPC4-dependent manner<sup>32</sup>, suggesting that this reservoir can be brought to distant sites by cell migration. Cytonemes, which are coated with glypicans<sup>33</sup>, could similarly boost the mobility of the Wnt reservoir by allowing cell membranes carrying signalling-competent Wnt to reach distant sites more rapidly. The capacity of this reservoir could readily be modulated by changes in expression or activity of Dlp class glypicans, perhaps explaining why the range of Wnt proteins differs in various contexts.

## Online content

Any methods, additional references, Nature Research reporting summaries, source data, extended data, supplementary information, acknowledgements, peer review information; details of author contributions and competing interests; and statements of data and code availability are available at <https://doi.org/10.1038/s41586-020-2498-z>.

- Willert, K. et al. Wnt proteins are lipid-modified and can act as stem cell growth factors. *Nature* **423**, 448–452 (2003).
- Takada, R. et al. Monounsaturated fatty acid modification of Wnt protein: its role in Wnt secretion. *Dev. Cell* **11**, 791–801 (2006).
- Janda, C. Y., Waghray, D., Levin, A. M., Thomas, C. & Garcia, K. C. Structural basis of Wnt recognition by Frizzled. *Science* **337**, 59–64 (2012).
- Pančková, D., Sprong, H., Marois, E., Thiele, C. & Eaton, S. Lipoprotein particles are required for Hedgehog and Wingless signalling. *Nature* **435**, 58–65 (2005).
- Gross, J. C., Chaudhary, V., Bartscherer, K. & Boutros, M. Active Wnt proteins are secreted on exosomes. *Nat. Cell Biol.* **14**, 1036–1045 (2012).
- Mulligan, K. A. et al. Secreted Wingless-interacting molecule (Swim) promotes long-range signaling by maintaining Wingless solubility. *Proc. Natl Acad. Sci. USA* **109**, 370–377 (2012).
- Kiecker, C. & Niehrs, C. A morphogen gradient of Wnt/ $\beta$ -catenin signalling regulates anteroposterior neural patterning in *Xenopus*. *Development* **128**, 4189–4201 (2001).
- Farin, H. F. et al. Visualization of a short-range Wnt gradient in the intestinal stem-cell niche. *Nature* **530**, 340–343 (2016).
- Alexandre, C., Baena-Lopez, A. & Vincent, J. P. Patterning and growth control by membrane-tethered Wingless. *Nature* **505**, 180–185 (2014).
- Tian, A., Duwadi, D., Benchabane, H. & Ahmed, Y. Essential long-range action of Wingless/Wnt in adult intestinal compartmentalization. *PLoS Genet.* **15**, e1008111 (2019).
- Zecca, M., Basler, K. & Struhl, G. Direct and long-range action of a wingless morphogen gradient. *Cell* **87**, 833–844 (1996).
- Harmansa, S., Hamaratoglu, F., Affolter, M. & Caussinus, E. Dpp spreading is required for medial but not for lateral wing disc growth. *Nature* **527**, 317–322 (2015).
- Yan, D., Wu, Y., Feng, Y., Lin, S. C. & Lin, X. The core protein of glypican Dally-like determines its biphasic activity in wingless morphogen signaling. *Dev. Cell* **17**, 470–481 (2009).
- Franch-Marro, X. et al. Glypicans shunt the Wingless signal between local signalling and further transport. *Development* **132**, 659–666 (2005).
- Stanganello, E. et al. Filopodia-based Wnt transport during vertebrate tissue patterning. *Nat. Commun.* **6**, 5846 (2015).
- Baeg, G. H., Selva, E. M., Goodman, R. M., Dasgupta, R. & Perrimon, N. The Wingless morphogen gradient is established by the cooperative action of Frizzled and Heparan Sulfate Proteoglycan receptors. *Dev. Biol.* **276**, 89–100 (2004).
- Reichsman, F., Smith, L. & Cumberledge, S. Glycosaminoglycans can modulate extracellular localization of the wingless protein and promote signal transduction. *J. Cell Biol.* **135**, 819–827 (1996).

18. Baena-Lopez, L. A., Franch-Marro, X. & Vincent, J. P. Wingless promotes proliferative growth in a gradient-independent manner. *Sci. Signal.* **2**, ra60 (2009).
19. Tang, X. et al. Roles of N-glycosylation and lipidation in Wg secretion and signaling. *Dev. Biol.* **364**, 32–41 (2012).
20. Kakugawa, S. et al. Notum deacylates Wnt proteins to suppress signalling activity. *Nature* **519**, 187–192 (2015).
21. Fuerer, C., Habib, S. J. & Nusse, R. A study on the interactions between heparan sulfate proteoglycans and Wnt proteins. *Dev. Dyn.* **239**, 184–190 (2010).
22. Mihara, E. et al. Active and water-soluble form of lipidated Wnt protein is maintained by a serum glycoprotein afamin/α-albumin. *eLife* **5**, e11621 (2016).
23. Kim, M. S., Saunders, A. M., Hamaoka, B. Y., Beachy, P. A. & Leahy, D. J. Structure of the protein core of the glypican Dally-like and localization of a region important for hedgehog signaling. *Proc. Natl Acad. Sci. USA* **108**, 13112–13117 (2011).
24. Pei, J. & Grishin, N. V. Cysteine-rich domains related to Frizzled receptors and Hedgehog-interacting proteins. *Protein Sci.* **21**, 1172–1184 (2012).
25. Hirai, H., Matoba, K., Mihara, E., Arimori, T. & Takagi, J. Crystal structure of a mammalian Wnt-frizzled complex. *Nat. Struct. Mol. Biol.* **26**, 372–379 (2019).
26. Awad, W. et al. Structural Aspects of N-Glycosylations and the C-terminal Region in Human Glypican-1. *J. Biol. Chem.* **290**, 22991–23008 (2015).
27. Sivasankaran, R., Calleja, M., Morata, G. & Basler, K. The Wingless target gene Dfz3 encodes a new member of the *Drosophila* Frizzled family. *Mech. Dev.* **91**, 427–431 (2000).
28. Schilling, S., Steiner, S., Zimmerli, D. & Basler, K. A regulatory receptor network directs the range and output of the Wingless signal. *Development* **141**, 2483–2493 (2014).
29. Mii, Y. & Taira, M. Secreted Frizzled-related proteins enhance the diffusion of Wnt ligands and expand their signalling range. *Development* **136**, 4083–4088 (2009).
30. Hayashi, Y., Kobayashi, S. & Nakato, H. *Drosophila* glypicans regulate the germline stem cell niche. *J. Cell Biol.* **187**, 473–480 (2009).
31. Wang, X. & Page-McCaw, A. A matrix metalloproteinase mediates long-distance attenuation of stem cell proliferation. *J. Cell Biol.* **206**, 923–936 (2014).
32. Serralbo, O. & Marcelle, C. Migrating cells mediate long-range WNT signaling. *Development* **141**, 2057–2063 (2014).
33. González-Méndez, L., Gradilla, A. C. & Guerrero, I. The cytoneme connection: direct long-distance signal transfer during development. *Development* **146**, dev174607 (2019).

**Publisher's note** Springer Nature remains neutral with regard to jurisdictional claims in published maps and institutional affiliations.

© The Author(s), under exclusive licence to Springer Nature Limited 2020

## Methods

### Data reporting

No statistical methods were used to predetermine sample size. The experiments were not randomized, and investigators were not blinded to allocation during experiments and outcome assessment.

### Immunostaining and microscopy

The following primary antibodies were used: guinea-pig anti-Senseless (1:1,000, gift from H. Bellen), rabbit anti-V5 (1:500, Cell Signalling), mouse anti-V5 (1:500, Invitrogen), rabbit anti-GFP (1:500, Abcam), mouse anti-Wingless (1:200, Hybridoma bank), anti-Hrs (1:250, DSHB), anti-ApoL (1:1,000, gift from S. Eaton), rat anti-HA (1:250, Roche, 3F10), anti-ubiquitin (1:1,000, EMD Millipore), guinea-pig anti-Distal-less (1:1,000, gift from R. S. Mann). Secondary antibodies used were Alexa 488, Alexa 555 and Alexa647 (1:500, Molecular Probes). Total and extracellular immunostaining of imaginal discs was performed as previously described<sup>20</sup>. Imaginal discs were mounted in Vectashield with DAPI (Vector Laboratories) and imaged using a Leica SP5 confocal microscope. Confocal images were processed with ImageJ (N.I.H.) and Photoshop CS5.1 (Adobe). Images were analysed using ImageJ to determine Mander's overlap coefficient and Pearson's correlation coefficient. Colocalization was measured where the morphotrap expression domain and the domain of GFP-Wingless overlap. Images were manually thresholded to remove background signal.

### *Drosophila* husbandry and clone induction

All crosses were performed at 25 °C except those to generate discs shown in Extended Data Figs. 1d, 2a, c, d, in which larvae were reared at 18 °C, the Gal80<sup>ts</sup> permissive temperature, and then shifted to 29 °C, the restrictive temperature for the indicated time (see figure legends).

### *Drosophila* genotypes

All lines are available upon request. Detailed *Drosophila* genotypes are listed Supplementary Table 1.

### Expression vectors for cultured *Drosophila* cells

*Drosophila* S2 or S2R+, obtained from the *Drosophila* Genomics Resource Centre (DGRC), were cultured at 25 °C in Schneider's medium plus L-glutamine (Sigma) containing 10% (v/v) fetal bovine serum (FBS; Life Technologies) and 0.1 mg ml<sup>-1</sup> Pen/Strep (Life Technologies). Cell lines were not authenticated, but were tested for, and free from, mycoplasma. To generate plasmids expressing V5-tagged forms of Dlp<sup>ΔGPI</sup> and Dlp<sup>core</sup>, amino acids 53–723 and 53–622 of Dlp was amplified from pOT2-Dlp (DGRC gold collection) adding a V5 tag (GKPIPPLLGLDST) at the C terminus and a BIP-signal peptide at the N terminus and inserted into pMT-V5-HisA (ThermoFisher). For Dlp(S168M)<sup>ΔGPI</sup>-V5, a gene fragment encoding a region around the point mutation was generated (Integrated DNA Technologies) and subcloned into pMT-Dlp<sup>ΔGPI</sup>-V5. To generate plasmids expressing V5-tagged Dally<sup>ΔGPI</sup> and Dally<sup>core</sup>, amino acids 1–600 and 1–546 of Dally were amplified from pUAST-secDally-Myc (DNA from H. Nakato) adding a V5 tag (GKPIPPLLGLDST) at the C terminus. SecCherry was generated by adding BIP-signal peptide at the N terminus and inserting it into pMT-V5-HisA. To generate V5-tagged Notum(S237A), Notum(S237A) cDNA was amplified, adding a V5 tag (GKPIPPLLGLDST) at the C terminus and cloned into pMT-V5-HisA. To generate pMT-GFP-Wg, GFP-IgG2 linker was placed after the signal peptide of Wingless. To generate GPC3<sup>ΔGPI</sup>-V5, amino acids 1–535 were amplified from a GPC3 (NM\_004484) human cDNA clone (Origene) adding a V5 tag at the C terminus. To generate GPC4<sup>ΔGPI</sup>-V5, amino acids 1–487 were amplified from a GPC4 (NM\_001448) human cDNA clone (Origene) adding a V5 tag at the C terminus. To generate GPC5<sup>ΔGPI</sup>-V5, amino acids 1–528 were amplified from a GPC5 (NM\_004466) human cDNA clone (Origene) adding a V5 tag at the C terminus. To generate GPC6<sup>ΔGPI</sup>-V5 amino acids

1–529 were amplified from a GPC6 (NM\_005708.3) human cDNA clone (Sino Biological) adding a V5 tag at the C terminus.

### Generation of transgenic flies

The *Swim*<sup>ko</sup> line was generated by deleting all three coding exons depicted in Extended Data Fig. 3b. The regions were replaced with a PAX-Cherry selection cassette, which was used to identify potential candidates, subsequently confirmed by PCR. The knockout line is homozygous viable and fertile with no apparent morphological phenotype. Two variants of morphotrap were generated. The nanobody Vhh4, preceded by a BIP signal peptide, was cloned in frame with the transmembrane region of CD8 and an intracellular HA tag and inserted into the pUAST vector, lines on the second and third chromosome were subsequently generated by random integration. The nanobody LaG16 was cloned in frame with the type II transmembrane protein NRT with a Myc tag as a spacer to generate NRT-Myc-LaG16, which was cloned into pUAS-attB and inserted into the attP2 landing site. GFP-Wingless(S239A) was generated by inserting full-length *GFP-wg[S239A]* cDNA along with 135 bp of 5' untranslated region (UTR) and 1,200 bp of 3' UTR into RIV{mini-white} and reintegrating it into the *wg*<sup>ko</sup> line<sup>9</sup>. The GFP was placed after the signal peptide and an IgG2 linker was inserted after the GFP. UAS-attB vectors encoding GPC3, GPC4, GPC5 and GPC6 were generated by amplifying coding regions from cDNA clones (see expression vectors for cultured *Drosophila* cells for more information on cDNA clones) and adding a V5 tag immediately after the signal peptides. The resulting UAS-attB vectors were inserted into the attP2 landing site. UAS-Dlp<sup>ΔGPI</sup>-V5 was generated by sub-cloning Dlp<sup>ΔGPI</sup>-V5 from pMT-Dlp<sup>ΔGPI</sup>-V5 into the UAS-attB vector and inserting it into the attP2 landing site. UAS-Dlp(S168M) was generated by sub-cloning a region encoding Dlp(S168M) from pMT-Dlp(S168M)<sup>ΔGPI</sup>-V5 into UAS-Dlp-HA (from S. Cohen) and inserting it into the attP2 landing site. UAS-Dlp(M175C/N367C)-HA, UAS-Dlp(F172T/F195Y)-HA and UAS-Dlp(R169E/T170N/Q171M/F172T)-HA were generated by sub-cloning gene fragments (synthesized by Integrated DNA Technologies) altered to encode the relevant mutations into UAS-Dlp-HA. UAS-Dally(E149R/N150T/M151Q/T152F)-HA was generated by sub-cloning a gene fragment (synthesized by Integrated DNA technologies) altered to encode the relevant mutations into pAct-Dally-HA and subsequently sub-cloning into UAS-attB. All Dlp and Dally transgenes were inserted into the attP2 landing site. Transgenic lines were generated in house or with BestGene.

### Immunoblotting and Immunoprecipitation

Cell lysates were produced using Triton extraction buffer (TEB): 50 mM Tris pH 7.5, 150 mM NaCl, 1 mM EDTA, 1% Triton X-100. Cells were incubated in TEB for 10 min on ice then spun at 14,000 rpm for 10 min at 4 °C to remove remaining cell debris. Samples were run on 4–12% Bis-Tris NuPAGE gels (Invitrogen) with MES buffer. Proteins on gel were transferred onto nitrocellulose membrane using Biorad gel transfer System (Invitrogen). The membranes were washed with dH<sub>2</sub>O and blocked with 5% skimmed milk in 0.1% Tween-20 PBS (PBS-T) for 30 min at room temperature. Membranes were incubated with primary antibodies (mouse monoclonal anti-V5 (Life Technologies, 1:5,000), rabbit anti-GFP (Abcam, 1:5,000), anti-β-tubulin (DSHB, 1:2,000) and anti-Cherry (Abcam, 1:3,000) diluted in 5% milk PBS-T overnight at 4 °C and washed with PBS-T three times before incubation with 680RD- or 800CW-conjugated secondary antibodies (anti-mouse or anti-rabbit; LI-COR, 1:7,000). Membranes were washed again in PBS-T and 0.02% SDS, developed using an Odyssey Clx western blotting detection system (LI-COR). Uncropped western blot images can be found in Supplementary Fig. 1.

For peptide immunoprecipitations S2 cells were transiently transfected with Dlp<sup>core</sup>-V5, Dally<sup>core</sup>-V5 or Notum(S237A)-V5. Seventy-two hours later, medium was collected and spun at 14,000 rpm for 10 min at 4 °C to remove cell debris. Biotinylated palmitoleoylated and biotinylated non-palmitoleoylated Wingless peptides resuspended in 10 mM

## Article

Tris-HCl, pH 8, 35 mM NaCl and 10% DMSO were added to the cleared medium at a final concentration of 10  $\mu$ M and incubated for 8 h at 4 °C. Neutravidin beads were added and incubated overnight at 4 °C. Beads were then washed in wash buffer (10 mM Tris-HCl, pH 8, 35 mM NaCl) four times and protein was subsequently eluted from the beads by boiling in LDS sample buffer for 5 min.

### Topflash signalling assay

S2R+ cells were plated in 60 cm dish and transfected with 1  $\mu$ g of a plasmid containing a Wingless-responsive promoter driving Firefly luciferase and a ubiquitous Copia promoter driving *Renilla* luciferase (made by C. Alexandre). After 48 h, the S2R+ cells were counted and 1  $\times 10^6$  cells were plated in each well of a 12-well plate and allowed to attach. After 6 h, the medium was removed and replaced with concentrated conditioned medium (20 $\times$ ). After 24 h of treatment, the cells were lysed using cold passive lysis buffer (Promega), Firefly and *Renilla* luciferase levels were measured using the Dual Luciferase Reporter Assay System (Promega) and the Firefly/*Renilla* ratio was calculated to give the Wingless signalling activity. Each condition was tested in triplicate and the experiment was repeated four times.

### Large scale expression and purification of Dlp<sup>core</sup> wild-type and Dally<sup>core</sup>

The cDNA coding for *Drosophila melanogaster* Dlp<sup>core</sup> (residues D74-Q617, UNIPROT ID: Q9VUG1; this is slightly different from the Dlp<sup>core</sup> described above, P53-Y622) was cloned into pHR-CMV-TetO2\_3C-Twin-Strep\_IRES-EmGFP Addgene 113884: the plasmid encodes the protein of interest adding a Human Rhinovirus (HRV) 3C Protease-cleavable Twin-Strep tag at the C terminus, and allows both transient expression and lentiviral-based transduction of target cells<sup>34</sup>.

Dlp contains one canonical and one cryptic furin cleavage site at position 397 and 437, respectively. To produce homogenous batches of protein and to account for potential effects of furin processing on lipid binding, two protein forms were generated, one wild-type form containing the native furin cleavage site and one form where both furin sites were destroyed (K398Q, K399A, R402Q, R438Q, R441A). No difference in lipid binding behaviour was observed between these two forms. For crystallization purposes, the furin mutant form was used.

The protein was expressed, secreted in the culture medium, either by transient transfection of HEK293S GnTI(-) cells or by lentiviral transduction of HEK293S GnTI(-) TetR cells<sup>35</sup> (which allow doxycycline-controlled inducible expression) according to published protocols<sup>34,36</sup>. In the latter case, expression was induced using 1  $\mu$ g ml<sup>-1</sup> of doxycycline for 96 h at 37 °C. For transient transfection, conditioned medium was collected seven days post-transfection.

In both cases, collected conditioned medium was dialysed against 50 mM Tris-HCl, pH 8, 200 mM NaCl using a QuixStand bench-top system (GE Healthcare) connected to a 60 cm Xampler Cartridge (GE Healthcare) with a 10-kDa nominal MWCO. Initial purification was performed by Strep-tag affinity chromatography (StreptactinXT High Capacity column, IBA Lifesciences). In brief, the protein was loaded overnight with continuous circulation on the column, before being eluted in 100 mM Tris-HCl, pH 8, 150 mM NaCl, 1 mM EDTA, 50 mM biotin. The protein was further purified by size-exclusion chromatography (SEC) (Superdex 200 Increase 10/300 GL column, GE Healthcare) in a final buffer containing 10 mM Tris-HCl, pH 8, 35 mM NaCl. Between the affinity chromatography and SEC steps, the Twin-Strep-tag was removed by incubation for 48 h at 4 °C with HRV 3C Protease, added at a 1:50 (w/w) protease:glypican ratio.

*Drosophila melanogaster* Dally<sup>core</sup> (residues 65–541, Uniprot ID: Q24114), fused C-terminally with a hexa-histidine (6 $\times$ His) tag, was cloned into the pHLsec vector and expressed by transient transfection in HEK293T cells in the presence of the class I  $\alpha$ -mannosidase inhibitor, kifunensine<sup>36,37</sup>. Conditioned medium was collected five days after

transfection. Medium was concentrated and diafiltrated as before into 25 mM phosphate pH 8, 250 mM NaCl. The protein was incubated with TALON beads for 1 h at 16 °C. Beads were washed with 25 mM phosphate pH 8, 250 mM NaCl, followed by washes in wash buffer containing 5 mM imidazole. The protein was eluted in wash buffer containing 250 mM imidazole. Samples were subjected to SEC using a Superdex 200 16/60 column (GE Healthcare) equilibrated in 10 mM HEPES pH 7.5, 150 mM NaCl.

Man(5)GlcNAc(2) and Man(5–9)GlcNAc(2) residual glycosylation produced by expression in GnTI(-) HEK293S or by HEK293T cells with kifunensine, respectively, was preserved for biophysical and HPLC analysis of protein-lipid interaction, while the samples for crystallization were further deglycosylated by *in situ* deglycosylation by endo- $\beta$ -N-acetylglucosaminidase F1 treatment<sup>37</sup>.

### Peptide synthesis

All reagents were purchased from commercial sources (VWR, Fisher Scientific, Novabiochem, Fluorochem) and used without further purification.

**Synthesis of dmWg S239 ox Bio (CH<sub>3</sub>CO-KC(S)-HGMSGSC(S)-TVLK-(EDA)-Bio) and dmWg S239 (C16:1) ox Bio (CH<sub>3</sub>CO-KC(S)-HGMS(-C = O-(CH<sub>2</sub>)<sub>7</sub>CH = CH(CH<sub>2</sub>)<sub>5</sub>CH<sub>3</sub>)GSC(S)-TVLK-(EDA)-Bio).** Solid-phase synthesis took place on an Activotec P-11 peptide synthesizer (Activotec) using a Fmoc-Biotin NovaTag resin (0.2 mmol; Merck) and *N*( $\alpha$ )-Fmoc amino acids, including Fmoc-Ser-OH (Merck). Fmoc-Ser-OH was incorporated at the palmitoleoylation site. HATU was used as the coupling reagent with 5-fold excess of amino acids. Acetylation of the N-terminal of the peptide took place on the synthesizer by activation of acetic acid. Following chain assembly, the peptidyl resin was split into two portions of approximately one third and two thirds.

For dmWg S239 ox Bio, the peptide was cleaved from the resin and protecting groups removed by addition of a cleavage solution (95% trifluoroacetic acid (TFA), 2.5% H<sub>2</sub>O, 2.5% TIS). After 2 h, the resin was removed by filtration and peptides were precipitated with diethyl ether on ice. The peptide was isolated by centrifugation, then dissolved in H<sub>2</sub>O and freeze dried overnight. Next, disulfide bridge formation was as follows. Clear-Ox (Peptides International) resin (3 eq, 0.109 mmol, 330 mg of 0.33 mmol g<sup>-1</sup>) was conditioned by swelling in dichloromethane (DCM) for 40 min, then washed with dimethylformamide; HATU, 1-[bis(dimethylamino)methylene]-1*H*-1,2,3-triazolo[4,5-*b*]pyridinium 3-oxid hexafluorophosphate (DMF), methanol and water. The peptide (0.036 mmol, 60 mg) was dissolved in 10 ml of deionized water, added to the resin, then reacted at room temperature with gentle agitation for 2 days. After filtration to remove the resin and freeze drying, portions of the peptide were purified on a C8 reverse phase HPLC column (Agilent PrepHT Zorbax 300SB-C8, 21.2 $\times$ 250 mm, 7 m) using a linear solvent gradient of 10–50% acetonitrile (0.08% TFA) in H<sub>2</sub>O (0.08% TFA) over 40 min at a flow rate of 8 ml min<sup>-1</sup>. The peak fraction was analysed by LC-MS on an Agilent 1100 LC-MSD. The calculated molecular weight of the peptide was in agreement with the mass found. Calculated molecular mass: 1,657.65, actual mass: 1,657.65.

For dmWg S239 (C16:1) ox Bio, the peptidyl resin was palmitoleoylated as follows. Palmitoleoyl chloride (20 eq, 3 mmol, 903  $\mu$ l) was added to DMF (6 ml) and the solution added to the peptidyl resin (0.15 mmol). *N,N*-diisopropylethylamine (DMAP) (0.1 eq, 2 mg) was dissolved in 2.25 ml pyridine and added to resin. Following reaction at room temperature, 16 h, gentle agitation, the peptidyl resin was washed with 3 $\times$ DMF and 2 $\times$ DCM. The palmitoleoylated peptide was cleaved from the resin and protecting groups removed by addition of a cleavage solution (95% TFA, 2.5% H<sub>2</sub>O, 2.5% TIS). After 1 h, the resin was removed by filtration and peptides were precipitated with diethyl ether on ice. The peptide was isolated by centrifugation, then dissolved in H<sub>2</sub>O and freeze dried overnight. Next, disulfide bridge formation was as follows. Clear-Ox (Peptides International) resin (3 eq, 0.127 mmol, 384

mg of 0.33 mmol g<sup>-1</sup>) was conditioned by swelling in DCM for 40 min, then washed with DMF, methanol and water. The peptide (0.042 mmol, 80 mg) was dissolved in 10 ml of deionized water, added to the resin, then reacted at room temperature with gentle agitation for 3 days. After filtration to remove the resin and freeze drying, portions of the peptide were purified on a C8 reverse phase HPLC column (Agilent PrepHT Zorbax 300SB-C8, 21.2×250 mm, 7 m) using a linear solvent gradient of 5–100% MeCN (0.08% TFA) in H<sub>2</sub>O (0.08% TFA) over 40 min at a flow rate of 8 ml min<sup>-1</sup>. The peak fraction was analysed by LC–MS on an Agilent 1100 LC-MSD. The calculated molecular mass of the peptide was in agreement with the mass found. Calculated molecular mass: 1,894.33, actual mass: 1,894.27.

**Synthesis of mmWNT7A 204-213 S206 C16:1 ox Bio NH<sub>2</sub>-K(Cys-Ser-) HGV(Ser-palmitoleoyl)GS(Cys-Ser-)TTKT-PEG-Bio.** Solid-phase synthesis took place on an Activotec P-II peptide synthesizer (Activotec) using a Fmoc-PEG-Biotin NovaTag resin (0.2 mmol; Merck) and N(α)-Fmoc amino acids, including Fmoc-Ser-OH (Merck) and Boc-Lys(Boc)-OH (Fluorochem). Fmoc-Ser-OH was incorporated at the palmitoleoylation site and Boc-Lys(Boc)-OH was incorporated at the N-terminal. HATU was used as the coupling reagent with 5-fold excess of amino acids. The peptidyl resin was palmitoleoylated as follows. Palmitoleoyl chloride (20 eq, 1.5 mmol, 452 μl) was added to DMF (6 ml) and the solution added to the peptidyl resin (0.075 mmol). DMAP (0.1 eq, 1 mg) was dissolved in 2.25 ml pyridine and added to resin. Following reaction at room temperature, 16 h, gentle agitation, the peptidyl resin was washed with 3×DMF and 2×DCM. The palmitoleoylated peptide was cleaved from the resin and protecting groups removed by addition of a cleavage solution (95% TFA, 2.5% H<sub>2</sub>O, 2.5% TIS). After 1 h, the resin was removed by filtration and peptides were precipitated with diethyl ether on ice. The peptide was isolated by centrifugation, then dissolved in H<sub>2</sub>O and freeze dried overnight. Next, disulfide bridge formation was as follows. Clear-Ox (Peptides International) resin (3 eq, 0.147 mmol, 700 mg of 0.21 mmol g<sup>-1</sup>) was conditioned by swelling in DCM for 40 min, then washed with DMF, methanol and water. The peptide (0.049 mmol, 96 mg) was dissolved in 10 ml of deionized water, added to the resin, then reacted at room temperature with gentle agitation for 3 days. After filtration to remove the resin and freeze drying, portions of the peptide were purified on a C8 reverse phase HPLC column (Agilent PrepHT Zorbax 300SB-C8, 21.2 × 250 mm, 7 m) using a linear solvent gradient of 10–75% acetonitrile (0.08% TFA) in H<sub>2</sub>O (0.08% TFA) over 40 min at a flow rate of 8 ml min<sup>-1</sup>. The peak fraction was analysed by LC–MS on an Agilent 1100 LC-MSD. The calculated molecular weight of the peptide was in agreement with the mass found. Calculated molecular mass: 1,971.39, actual mass: 1,969.90.

**Synthesis of mmWNT7A 201-213 S206 ox C16:1 NH<sub>2</sub>-K(Cys-Ser-) HGV(Ser-16:1) GS(Cys-Ser-)TTKT-COOH.** Solid-phase synthesis took place on an Activotec P-II peptide synthesizer (Activotec) using a Fmoc-Thr(tBu)-Wang resin LL (0.2 mmol; Merck) and N(α)-Fmoc amino acids, including Fmoc-Ser-OH, Fmoc-Cys(MMT)-OH, Fmoc-Gly-Ser(ψMe, Mepro)-OH (all Merck) and Boc-Lys(Boc)-OH (Fluorochem). Fmoc-Ser-OH was incorporated at the palmitoleoylation site and Boc-Lys(Boc)-OH was incorporated at the N-terminal. HATU was used as the coupling reagent with 5-fold excess of amino acids. Palmitoleoyl chloride (18.5 eq, 3.7 mmol, 1,000 μl) was added to DMF (4 ml) and the solution added to the peptidyl resin (0.075 mmol). DMAP (0.1 eq, 2.5 mg) was dissolved in 2.50 ml pyridine and added to resin. Following reaction at room temperature, 16 h, gentle agitation, the peptidyl resin was washed with 3× DMF and 2× DCM. Next, formation of the disulfide bridge on the resin was performed as follows. Methoxytrityl was removed from the two cysteine residues by treatment of the peptidyl resin for 2 min with 10 ml of 1% TFA, 5% triisopropylsilane (TIS), rest DCM, then washed with DCM. This was repeated seven times

more. Next, the peptidyl resin was treated with *N*-chlorosuccinimide (1 eq) in 10 ml DMF for 10 min then washed with 3× DMF and 2× DCM. The palmitoleoylated, disulfide-bridged peptide was cleaved from the resin and protecting groups removed by addition of a cleavage solution (95% TFA, 2.5% H<sub>2</sub>O, 2.5% TIS). After 1 h, the resin was removed by filtration and peptides were precipitated with diethyl ether on ice. The peptide was isolated by centrifugation, then dissolved in H<sub>2</sub>O and freeze dried overnight. Portions of the peptide were purified on a C8 reverse phase HPLC column (Agilent PrepHT Zorbax 300SB-C8, 21.2×250 mm, 7 m) using a linear solvent gradient of 20–90% acetonitrile (0.08% TFA) in H<sub>2</sub>O (0.08% TFA) over 40 min at a flow rate of 8 ml min<sup>-1</sup>. The peak fraction was analysed by LC–MS on an Agilent 1100 LC-MSD. The calculated molecular mass of the peptide was in agreement with the mass found. Calculated molecular mass: 1542.00, actual mass: 1541.85.

**Synthesis of mmWNT7A 201-213 S206 ox C16:1 NH<sub>2</sub>-K(Cys-Ser-) HGV(Ser-16:1) GS(Cys-Ser-)TTKT-COOH.** Solid-phase synthesis took place on an Activotec P-II peptide synthesizer (Activotec) using a Fmoc-PEG-Biotin NovaTag resin (100 μmol; Merck) and N(α)-Fmoc amino acids, including Fmoc-Cys(MMT)-OH, Fmoc-Gly-Ser(ψMe, Mepro)-OH (all Merck) and Boc-Lys(Boc)-OH (Fluorochem). The first Fmoc-Thr(tBu)-OH was double coupled. Boc-Lys(Boc)-OH was incorporated at the N-terminal. HATU was used as the coupling reagent with 5-fold excess of amino acids. Following chain assembly, disulfide bridge formation on the resin was performed as follows. Methoxytrityl was removed from the two cysteine residues by treatment of the peptidyl resin for 2 min with 10 ml of 1% TFA, 5% TIS, rest DCM, then washed with DCM. This was repeated seven more times. Next, the peptidyl resin was treated with *N*-chlorosuccinimide (1 eq) in 10 ml DMF for 10 min then washed with 3× DMF and 2× DCM. The disulfide-bridged peptide was cleaved from the resin and protecting groups removed by addition of a cleavage solution (95% TFA, 2.5% H<sub>2</sub>O, 2.5% TIS). After 1 h, the resin was removed by filtration and peptides were precipitated with diethyl ether on ice. The peptide was isolated by centrifugation, then dissolved in H<sub>2</sub>O and freeze dried overnight. Portions of the peptide were purified on a C8 reverse phase HPLC column (Agilent PrepHT Zorbax 300SB-C8, 21.2x250 mm, 7 m) using a linear solvent gradient of 10–50% MeCN (0.08% TFA) in H<sub>2</sub>O (0.08% TFA) over 40 min at a flow rate of 8 ml min<sup>-1</sup>. The peak fraction was analysed by LC–MS on an Agilent 1100 LC-MSD. The calculated molecular mass of the peptide was in agreement with the mass found. Calculated molecular mass: 1,734.99, actual mass: 1,733.99.

### Bilayer interferometry

Data were collected with Octet RED96 and Octet RED384 instruments (FortéBio). All steps were performed in 10 mM Tris, 35 mM NaCl, pH 8 at 25 °C. Initially, Dip and Read Streptavidin Biosensors (FortéBio) were activated by dipping them in buffer for 10 min before starting the analysis. Sensors were then loaded with 0.05 mg ml<sup>-1</sup> of biotinylated palmitoleoylated and non-palmitoleoylated human WNT7A peptide. After baseline reference collection in wells containing only buffer, biosensors were dipped in analyte dilution series, before allowing dissociation in the same buffer wells where the baseline reference was collected. Peptide-loaded sensors tested against buffer were used for blank subtraction. Unloaded sensors dipped into the analyte dilution series were used as reference to account for non-specific binding.

Upon reference subtraction, data were analysed by the FortéBio (v.11.1) and SigmaPlot (v.14.0) data analysis software. The model used for curve fitting in kinetic and steady-state analysis was a 1:1 Langmuir binding isotherm model. Data were collected in three independent experiments.

### Crystallization, data collection and structure determination

Purified proteins were concentrated by ultrafiltration to 3.5 mg ml<sup>-1</sup> and incubated for 16 h at 4 °C with palmitoleoylated human WNT7A

peptide (resuspended in 10 mM Tris-HCl, pH 8, 35 mM NaCl and added at a final concentration of 5 mM). After incubation, 96-well crystallization plates were set up at 20 °C using a Cartesian Technologies pipetting robot dispensing nanolitre-scale drops consisting of 100 nl of protein solution and 100 nl of reservoir solution<sup>38</sup>. Crystals appeared after 2 weeks in a variety of conditions with 20% (w/v) PEG4000 as precipitant and different pH values.

Prior to crystal freezing, crystals were additionally soaked with palmitoleoylated human WNT7A peptide resuspended in DMSO, at a final concentration of 1 mM peptide in 10% (v/v) DMSO. The crystals were soaked for 1 h before flash-cooling by dipping into liquid nitrogen, using mother liquor supplemented with 25% (v/v) glycerol as cryoprotectant.

Because initial crystals diffracted at 3 Å with a high degree of anisotropy in the *c*\* dimension, optimization of the crystal growth was performed, designing a two-dimensional pH/precipitant screening matrix (5–9 pH interval using 0.1 M monomethoxytrityl (MMT)<sup>39</sup> buffer, 15–25% w/v PEG4000 concentration interval). The best diffracting crystals grew in 16.25% (w/v) PEG4000, 0.1 M MMT pH 9.

Data were collected at 100 K at Diamond Light Source beamline i04 equipped with an Eiger2X 16M detector using a wavelength of 0.9795 Å.

Data were processed using Xia2<sup>40</sup>, scaled using DIALS<sup>41</sup> and merged using AIMLESS<sup>42,43</sup>.

The structure of Dlp<sup>core</sup> in complex with human WNT7A palmitoylated peptide was solved to a resolution of 2.21 Å by molecular replacement with PHASER<sup>44</sup> using the previously published apo-form of Dlp (PDB code 3odn)<sup>23</sup> as a search model. Iterative cycles of refinement and manual rebuilding were performed using phenix.refine<sup>45</sup> and COOT<sup>46</sup>. To avoid model bias, the WNT7A peptide model was added only at the latest stages of refinement. PEG was also present in the crystallization cocktail, however a number of reasons provided the rationale for fitting palmitoleate into the density: several types of omit maps, generated using phenix.refine and phenix.polder (Fig. 3c, Extended Data Fig. 8), show clear evidence of continuous electron density not only for the lipid part but also for the peptide moiety of the palmitoleoylated peptide; although crystallized in a different space group, PEG was also present in the crystallization cocktail of the published apo form and no conformational rearrangement and no lipid-like density is present in the latter; to fit the electron density, a fragment of PEG of the exact same dimensions as the palmitoleate would be required; the highly hydrophobic binding cavity is less compatible with a polar molecule such as PEG than with a lipid. Subsequent results for mutant DlpS showing reduced *in vitro* and *in vivo* lipid binding confirmed the identification of the pocket as the palmitoleate binding unit.

SMILES for the chemical structure of the peptide was designed using CHEMDRAW and peptide model and restraints for refinement were generated by the GRADE webserver<sup>47</sup>. Refinement models were validated with MOLPROBITY<sup>48</sup>. No Ramachandran outliers are present in the final model, with 97.83% of the residues in the favoured region of the Ramachandran plot. Data collection and refinement statistics are presented in Extended Data Table 1.

Inspection of crystal contacts revealed one in the region of the conformational change; however, Protein Interfaces, Surfaces and Assemblies (PISA) EMBL-EBI<sup>49</sup> server analysis reported this to be only a minor interface (554 Å<sup>2</sup> out of 22,260 Å<sup>2</sup> of accessible surface area), with a complex significance score (CSS) of 0, indicating that it is an energetically very weak interface and therefore not be expected to trigger a notable conformational rearrangement in the structure. Structural superpositions were performed in COOT, using the LSQ algorithm. Structural figures were created by PYMOL (v.2.2.0) and assembled using INKSCAPE. Sequence alignments were generated using JALVIEW<sup>50</sup> (v. 2.10.5). Lipid-binding cavity analysis and visualization were performed using CASTp<sup>51</sup> and its related PYMOL plugin.

## Large-scale expression and purification of mutants for *in vitro* binding analysis

Mutations were generated by a two-step overlapping PCR and mutants were cloned into the pHLSec vector encoding for C-terminal 6×His and AviTag tags<sup>52</sup>. The mutant Dlp forms were expressed by transient transfection of GntI(-) HEK293S, dialysed against 20 mM Tris, pH 8, 500 mM NaCl, 20 mM imidazole and initially purified by Ni-NTA affinity chromatography (HisTrap HP, GE Healthcare). Subsequently, proteins were further purified by SEC using the same experimental setting described for the wild-type protein.

## Protein-lipid binding tests by FSEC

Fluorescently labelled C16:0 palmitic acid bodipy FL C<sub>16</sub> (4,4-difluoro-5,7-dimethyl-4-bora-3a,4a-diaza-s-indacene-3-hexadecanoic acid, Sigma-Aldrich) was incubated with the proteins of interest for 16 h at 4 °C in 10 mM Tris-HCl, pH 8, 35 mM NaCl, 7.5% DMSO. The proteins were used at a concentration of 2 μM, and the fluorescent lipid was added at a 1:20 (w/w) protein:lipid ratio.

After incubation, the samples were run on a Superose 6 Increase 3.2/200 column in a FSEC Prominence HPLC system (Shimadzu) equipped with a RF-10AXL fluorescent detector. The running buffer was 10 mM Tris-HCl, pH 8, 35 mM NaCl. The runs were performed at a flow rate of 0.08 ml min<sup>-1</sup>. The fluorescent dye was excited at 505 nm and emission registered at 512 nm; absorbance at 280 nm was also registered to compare the elution profiles with those of the fluorescence emission. Bodipy FL C<sub>16</sub> in absence of proteins was run as control. Data were collected in three independent experiments.

## Reporting summary

Further information on research design is available in the Nature Research Reporting Summary linked to this paper.

## Data availability

X-ray crystallographic coordinates and structure factor files generated during the current study are available from the RCSB Protein Data Bank (PDB) under accession code 6XTZ. Full scans for all western blots are provided in Supplementary Fig. 1. Source data are provided with this paper.

34. Elegheert, J. et al. Lentiviral transduction of mammalian cells for fast, scalable and high-level production of soluble and membrane proteins. *Nat. Protocols* **13**, 2991–3017 (2018).
35. Reeves, P. J., Callewaert, N., Contreras, R. & Khorana, H. G. Structure and function in rhodopsin: high-level expression of rhodopsin with restricted and homogeneous *N*-glycosylation by a tetracycline-inducible *N*-acetylglucosaminyltransferase I-negative HEK293S stable mammalian cell line. *Proc. Natl Acad. Sci. USA* **99**, 13419–13424 (2002).
36. Aricescu, A. R., Lu, W. & Jones, E. Y. A time- and cost-efficient system for high-level protein production in mammalian cells. *Acta Crystallogr. D* **62**, 1243–1250 (2006).
37. Chang, V. T. et al. Glycoprotein structural genomics: solving the glycosylation problem. *Structure* **15**, 267–273 (2007).
38. Walter, T. S. et al. A procedure for setting up high-throughput nanolitre crystallization experiments. Crystallization workflow for initial screening, automated storage, imaging and optimization. *Acta Crystallogr. D* **61**, 651–657 (2005).
39. Newman, J. Novel buffer systems for macromolecular crystallization. *Acta Crystallogr. D* **60**, 610–612 (2004).
40. Winter, G., Lobley, C. M. & Prince, S. M. Decision making in xia2. *Acta Crystallogr. D* **69**, 1260–1273 (2013).
41. Winter, G. et al. DIALS: implementation and evaluation of a new integration package. *Acta Crystallogr. D* **74**, 85–97 (2018).
42. Evans, P. R. & Murshudov, G. N. How good are my data and what is the resolution? *Acta Crystallogr. D* **69**, 1204–1214 (2013).
43. Winn, M. D. et al. Overview of the CCP4 suite and current developments. *Acta Crystallogr. D* **67**, 235–242 (2011).
44. McCoy, A. J. et al. Phaser crystallographic software. *J. Appl. Crystallogr.* **40**, 658–674 (2007).
45. Afonine, P. V. et al. Towards automated crystallographic structure refinement with phenix.refine. *Acta Crystallogr. D* **68**, 352–367 (2012).
46. Emsley, P., Lohkamp, B., Scott, W. G. & Cowtan, K. Features and development of Coot. *Acta Crystallogr. D* **66**, 486–501 (2010).
47. Smart, O. S. *Grade v.1.105*; <http://grade.globalphasing.org> (2012).

48. Williams, C. J. et al. MolProbity: More and better reference data for improved all-atom structure validation. *Protein Sci.* **27**, 293–315 (2018).
49. Krissinel, E. & Henrick, K. Inference of macromolecular assemblies from crystalline state. *J. Mol. Biol.* **372**, 774–797 (2007).
50. Waterhouse, A. M., Procter, J. B., Martin, D. M., Clamp, M. & Barton, G. J. Jalview Version 2—a multiple sequence alignment editor and analysis workbench. *Bioinformatics* **25**, 1189–1191 (2009).
51. Tian, W., Chen, C., Lei, X., Zhao, J. & Liang, J. CASTp 3.0: computed atlas of surface topography of proteins. *Nucleic Acids Res.* **46** (W1), W363–W367 (2018).
52. Beckett, D., Kovaleva, E. & Schatz, P. J. A minimal peptide substrate in biotin holoenzyme synthetase-catalyzed biotinylation. *Protein Sci.* **8**, 921–929 (1999).
53. Port, F., Chen, H. M., Lee, T. & Bullock, S. L. Optimized CRISPR/Cas tools for efficient germline and somatic genome engineering in *Drosophila*. *Proc. Natl Acad. Sci. USA* **111**, E2967–E2976 (2014).
54. Liebschner, D. et al. Polder maps: improving OMIT maps by excluding bulk solvent. *Acta Crystallogr. D* **73**, 148–157 (2017).

**Acknowledgements** We thank C. Alexandre for plasmids and advice, J. Kurth for *Drosophila* injections, T. Walter for technical support with crystallization, and W. Lu and Y. Zhao for help with tissue culture and advice. We thank K. Harlos and staff at Diamond Light Source beamlines (i03, i04 and i04-1) for assistance with X-ray data collection (proposal MX19946).

This work was supported by core funding to the Francis Crick Institute to J.P.V. (CRUK FC001204, MRC FC001204, and Wellcome Trust FC001204), the European Union (ERC grants WNTEXPORT (294523) to J.P.V., and CilDyn (647278) to C.S.), Cancer Research UK (C375/A17721 to E.Y.J., and C20724/A26752 to C.S.). L.V. is supported by Wellcome Trust PhD Training Programme 102164/B/13/Z. The Wellcome Centre for Human Genetics is supported by Wellcome Trust Centre grant 203141/Z/16/Z.

**Author contributions** Experimental contributions were as follows: *Drosophila* developmental genetics and cell-based assays (I.J.M.), genetic analysis of LPPs (K.B.), biophysics and structural biology (L.V., B.B., T.M., C.S.); peptide synthesis (D.J., N.O'R.). The project was conceived by I.J.M., L.V., E.Y.J. and J.-P.V. The first draft of the paper was written by J.-P.V., E.Y.J., I.J.M. and L.V. All the authors contributed to the design and interpretation of experiments.

**Competing interests** The authors declare no competing interests.

**Additional information**

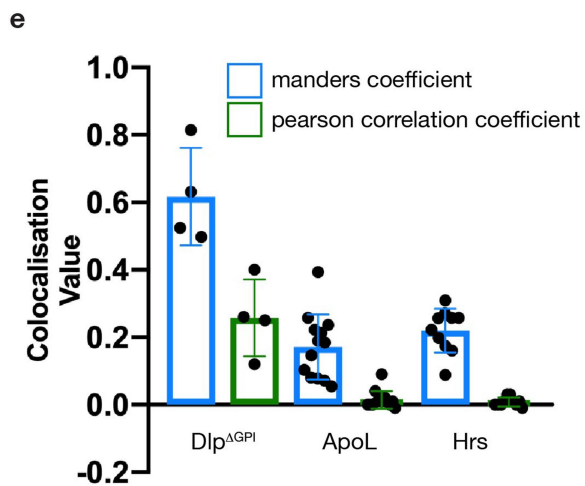
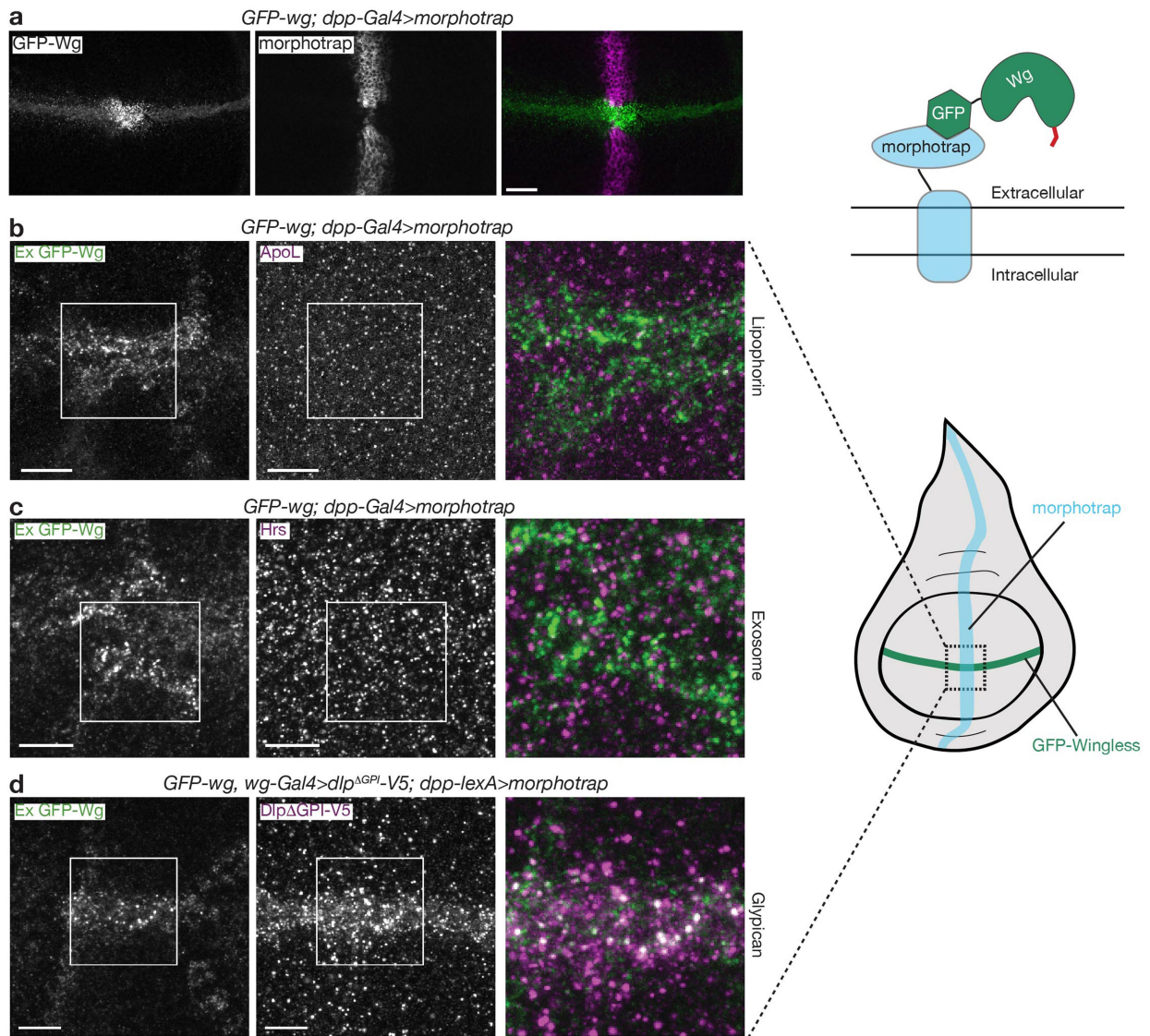
**Supplementary information** is available for this paper at <https://doi.org/10.1038/s41586-020-2498-z>.

**Correspondence and requests for materials** should be addressed to E.Y.J. or J.-P.V.

**Peer review information** *Nature* thanks Elina Ikonen, Daniel Leahy, Roeland Nusse and the other, anonymous, reviewer(s) for their contribution to the peer review of this work.

**Reprints and permissions information** is available at <http://www.nature.com/reprints>.

# Article

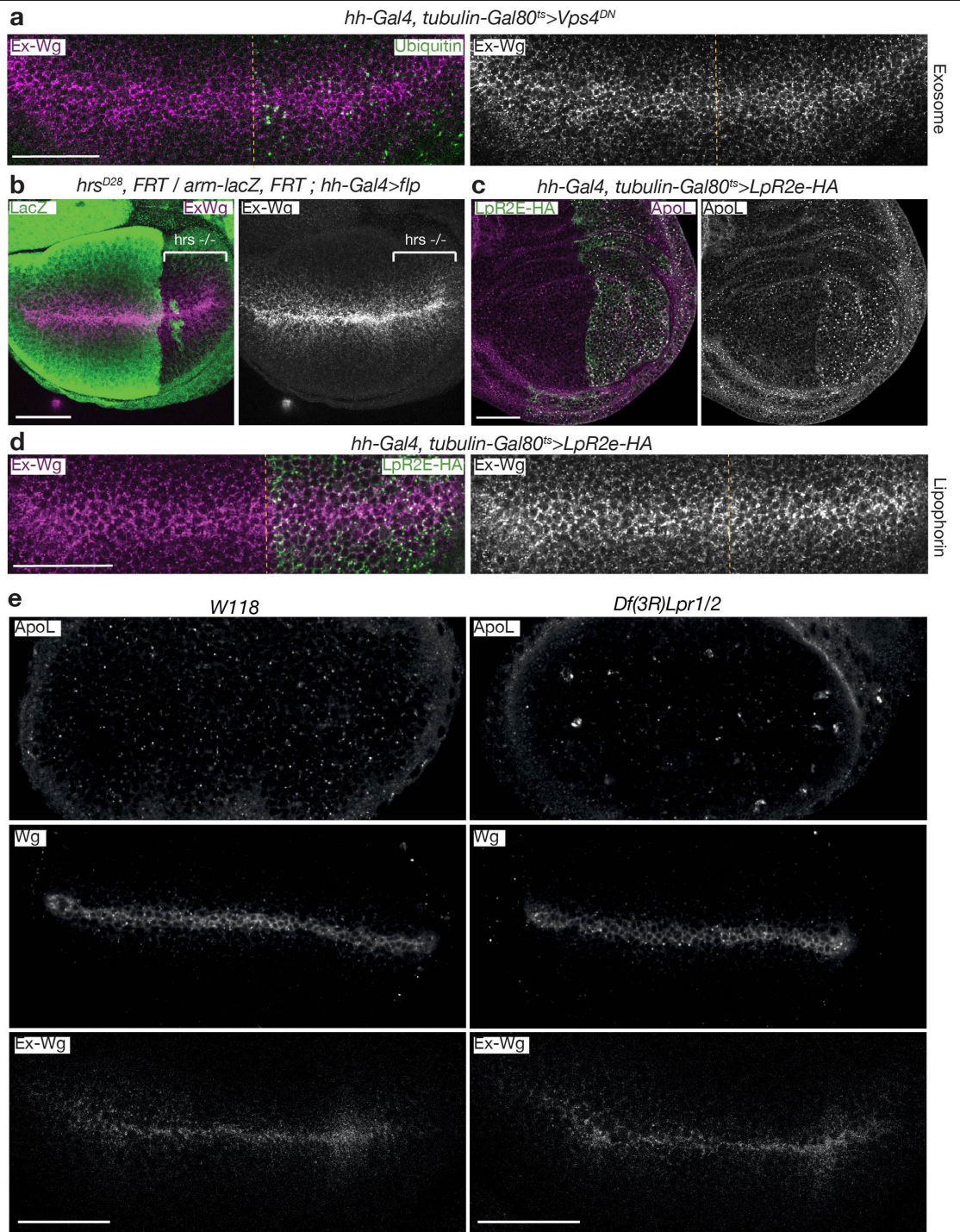
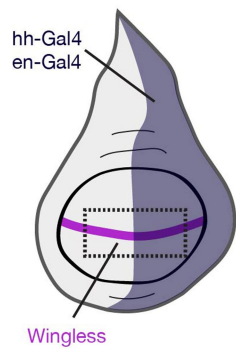


Extended Data Fig. 1 | See next page for caption.

**Extended Data Fig. 1 | Extracellular Wingless, captured by morphotrap, colocalizes with Dlp<sup>ΔGPI</sup> but not exosomes or lipophorin particles.**

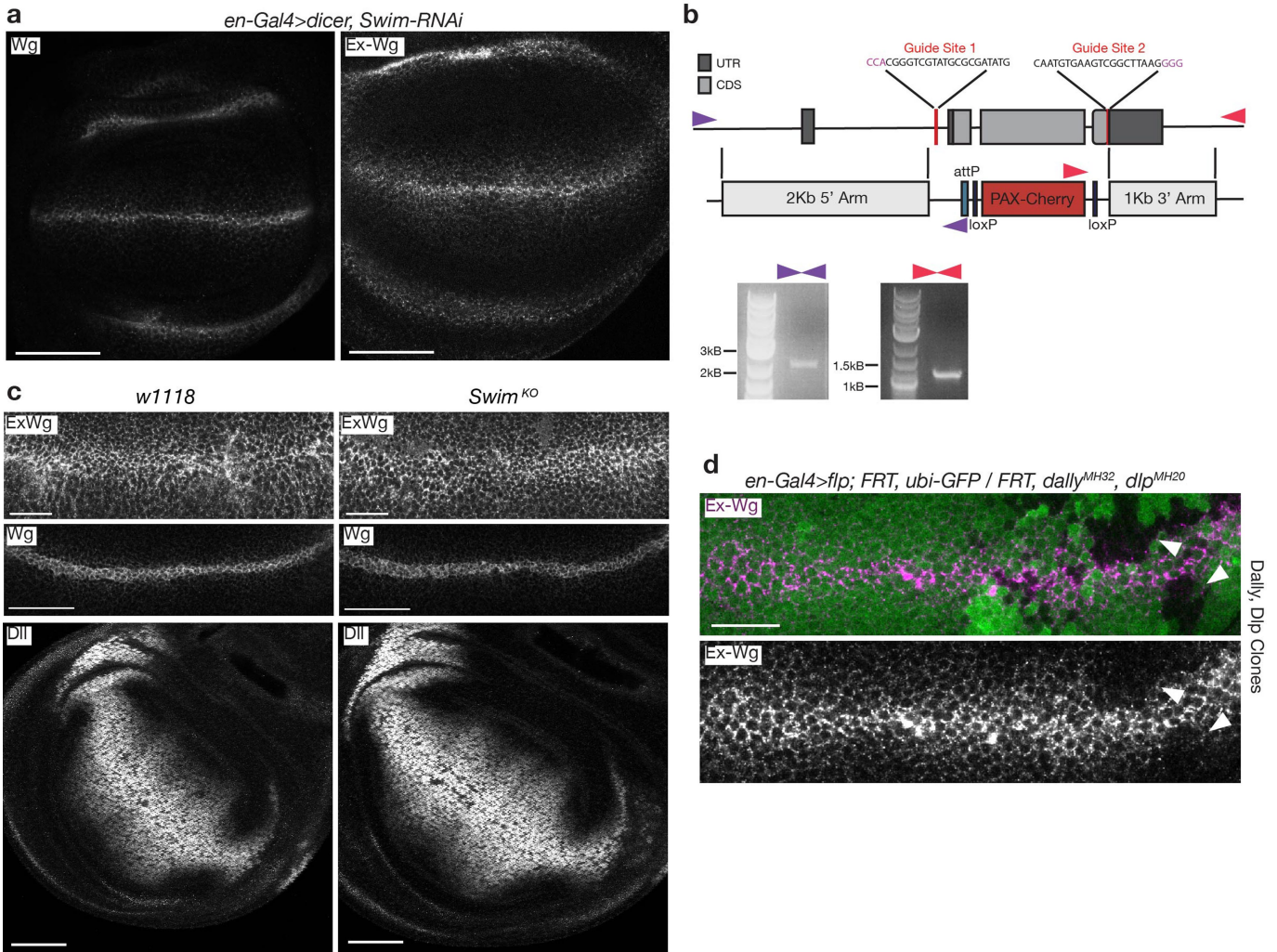
**a**, A membrane-tethered anti-GFP nanobody (Vhh4-CD8-HA, morphotrap), expressed in a transversal stripe with *dpp-Gal4*, leads to accumulation of GFP-Wingless (from a knock-in allele<sup>53</sup>) where the two expression domains overlap. The apparent gap in morphotrap expression is due to the known low activity of *dpp-gal4* there. Residual expression is nevertheless sufficient to trap GFP-Wingless. **b-d**, Immunofluorescent localization of morphotrap-enriched GFP-Wingless and endogenous ApoL or endogenous Hrs. **d**, Immunofluorescent

localization of morphotrap-enriched GFP-Wingless and overexpressed Dlp<sup>ΔGPI</sup>-V5. Here, morphotrap is expressed with *dpp-LexA* and Dlp<sup>ΔGPI</sup>-V5 with *wg-Gal4*. White colour indicates extensive colocalization. Dlp<sup>ΔGPI</sup>-V5 expression was limited to 24 h with Gal80<sup>ts</sup> to avoid pleiotropic effects. **e**, Colocalization was quantified where the morphotrap and GFP-Wingless expression domains intersect. Error bars denote s.d.  $n = 4$  (Dlp<sup>ΔGPI</sup>-V5),  $n = 13$  (ApoL) and  $n = 10$  (Hrs), in which  $n$  denotes number of wing discs. Scale bars, 50  $\mu\text{m}$  (**a**), 10  $\mu\text{m}$  (**b-d**). All experiments were repeated independently three times with similar results.



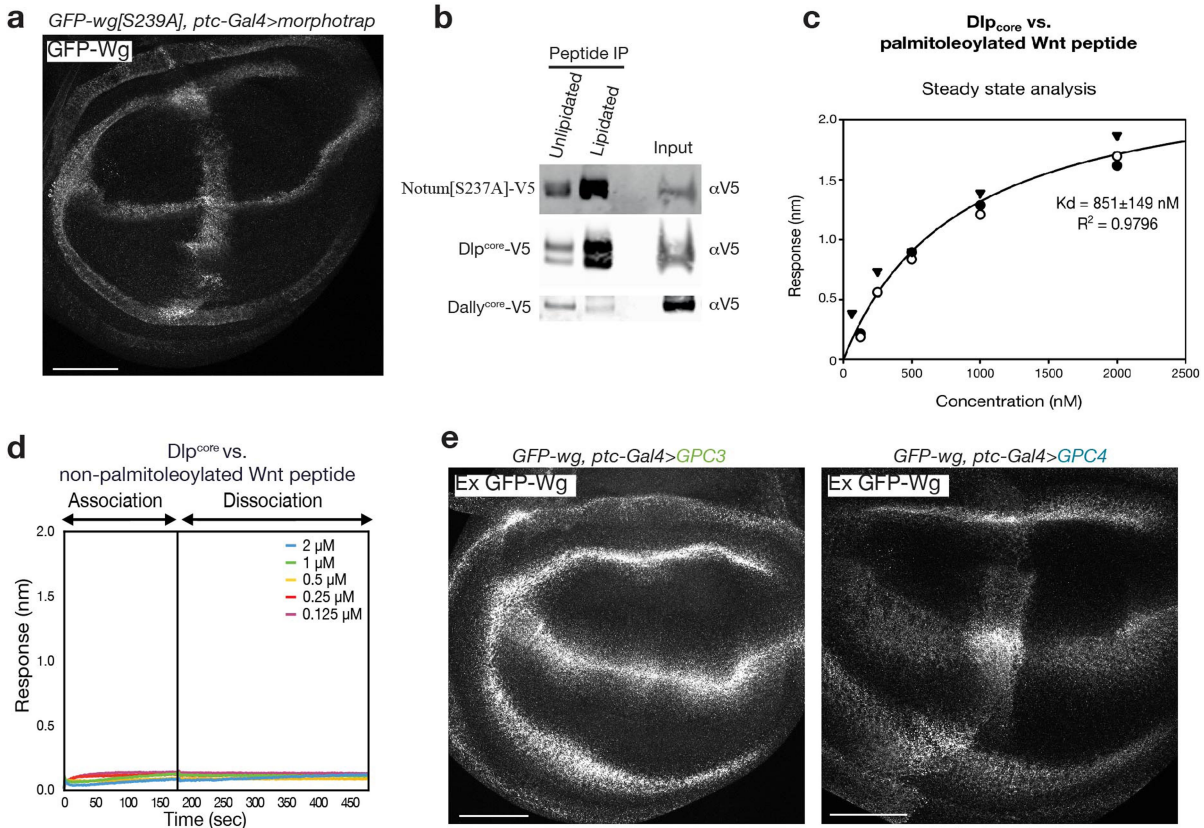
**Extended Data Fig. 2 | Genetic perturbation of exosomes or lipophorin particles does not alter the distribution of extracellular Wingless.**  
**a**, Expression of dominant-negative Vps4 with *hh-Gal4* in the posterior compartment (limited to 8 h with Gal80<sup>ts</sup> to avoid pleiotropic effects of sustained VPS4 inhibition) does not affect extracellular Wingless despite disruption of MVB formation indicated by accumulation of ubiquitin. Anterior compartment serves as a control. Dashed line denotes anterior posterior boundary. **b**, Expression of extracellular Wingless is largely unaffected by the loss of Hrs activity. The posterior compartment was rendered homozygous for

a null *hrs* mutation using the indicated genotype. **c, d**, Overexpression of the lipophorin receptor Lpr2E-HA for 24 h with the *hh-Gal4* driver increases the uptake of ApoL in the posterior compartment but has no effect on extracellular Wingless. The anterior compartment serves as a control. **e**, Extracellular Wingless and ApoL in wing discs from *w118* (control) or homozygotes for a deficiency that removes the two main lipophorin receptors Lpr1/2. The uptake of lipophorin is reduced in the deficiency line but neither total nor extracellular Wingless is altered. Scale bars, 50  $\mu$ m. All experiments were repeated independently three times with similar results.



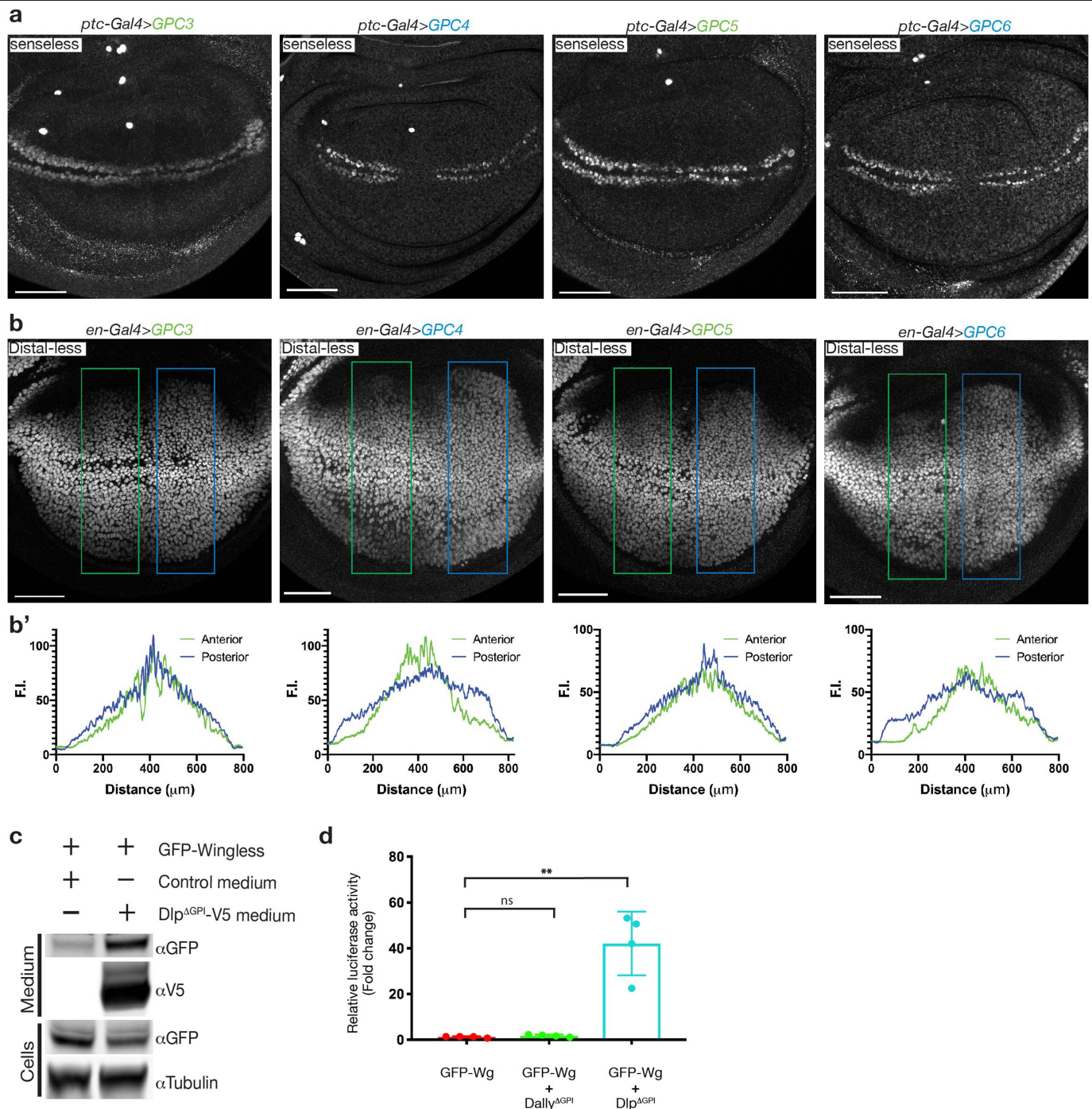
**Extended Data Fig. 3 | Genetic perturbation of Dlp and dally but not of Swim alters the distribution of extracellular Wingless.** **a**, Expression of an RNAi against *Swim* in the posterior compartment (*en-Gal4*) does not alter extracellular or total Wingless. Scale bar, 50  $\mu\text{m}$ . **b**, Schematic of the *Swim* locus and the CRISPR-Cas9 strategy used to delete the gene. Successful deletion was verified by PCR using two independent primer pairs indicated by purple and

red arrowheads. **c**, Extracellular Wingless and Distal-less expression in control (*w1118*) and *Swim<sup>KO</sup>* wing discs. Neither is altered after *Swim* deletion. Scale bars, 50  $\mu\text{m}$ . **d**, Extracellular Wingless is reduced in clones lacking both Dlp and Dally (marked by the absence of GFP (white arrowheads)). Scale bars, 25  $\mu\text{m}$ . All experiments were repeated independently three times with similar results.



**Extended Data Fig. 4 | Further evidence for the lipid binding activity of Dlp class glypicans.** **a**, GFP–Wingless(S239A) expressed from a knock-in allele is trapped by CD8–VHH expressed with *dpp-Gal4*. This result shows that GFP–Wingless(S239A) is secreted and can be captured in the extracellular space and thus serves as a positive control for Fig. 2a. Scale bars, 50  $\mu$ m. **b**, Dlp<sup>core</sup> and Notum(S237A), but not Dally<sup>core</sup>, preferentially bind a palmitoleoylated peptide (sequence from the Wingless protein). Biotinylated palmitoleoylated and non-palmitoleoylated peptides were incubated with medium from S2 cells expressing Dlp<sup>core</sup>-V5, Notum(S237A)-V5 or Dally<sup>core</sup>-V5. Biotinylated peptides were pulled down with streptavidin beads and the extent to which Dlp<sup>core</sup>, Notum(S237A)-V5 and Dally<sup>core</sup> are co-pulled down was determined by western blot. A peptide-based approach was used because of difficulties associated with the production of soluble Wingless protein. Binding was estimated from the amount of protein co-pulled down from conditioned medium by streptavidin beads. **c**, Steady-state analysis of the Dlp<sup>core</sup> versus

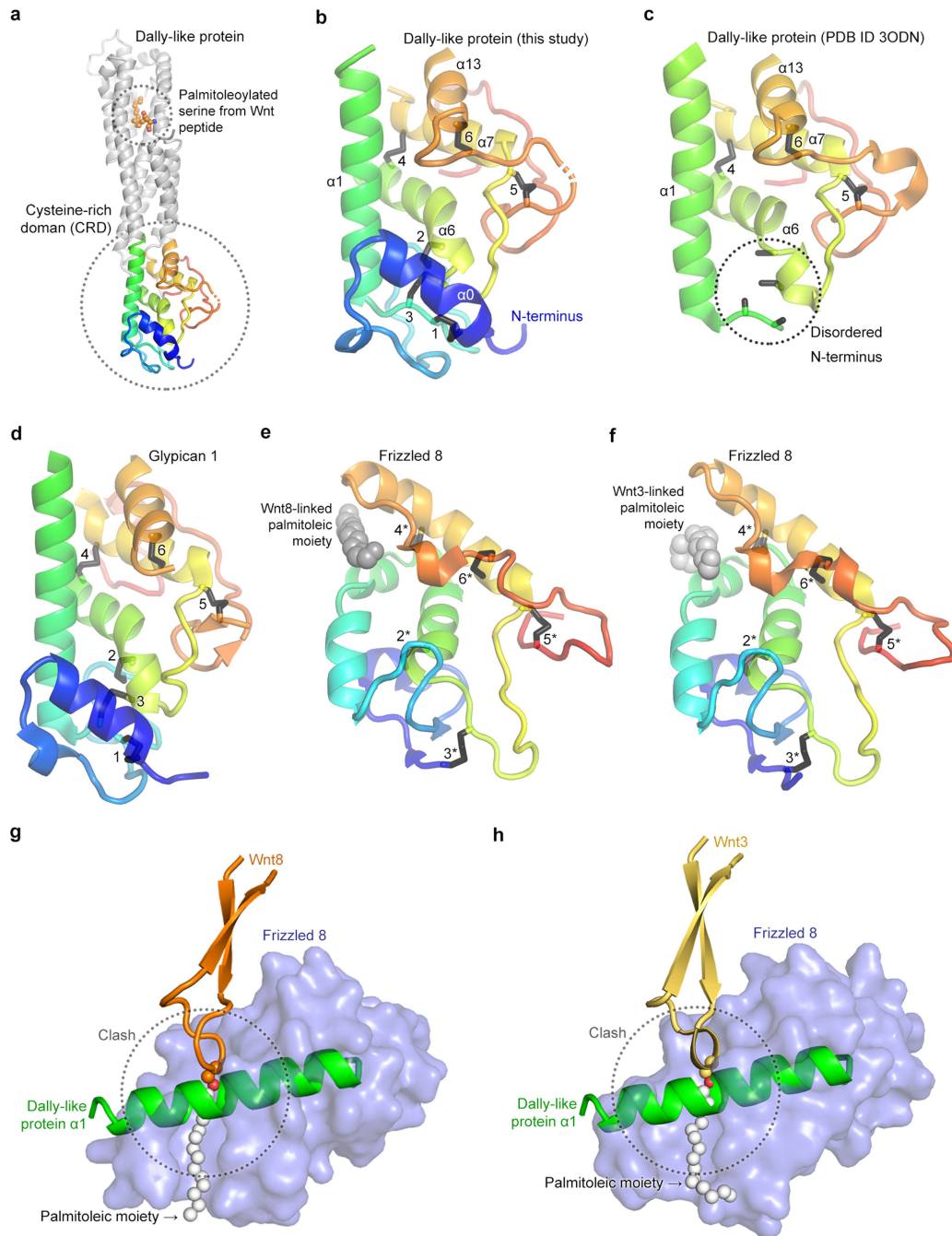
palmitoleoylated human WNT7A peptide interaction measured by BLI shown in Fig. 2b.  $K_d$  is calculated from a global fit of three independent experiments. Owing to the effect of non-specific binding on the shape of the binding isotherm curves (which could not be alleviated by detergents in light of the lipid-based nature of the interaction), we could not perfectly fit a 1:1 Langmuir model, therefore the indicated apparent dissociation constant is an estimate, not an exact value. **d**, Representative reference-subtracted BLI traces of Dlp<sup>core</sup> against biosensors loaded with non-palmitoleoylated peptide (sequence from relevant region of human WNT7A). No significant binding could be detected (compare to Fig. 2b). The experiments were repeated independently three times with similar results. **e**, Human GPC4 (Dlp family), but not human GPC3 (Dally family), expressed with *ptc-Gal4* captured GFP–Wingless at the cell surface. This panel extends the data of Fig. 2c. Scale bars, 50  $\mu$ m. All experiments were repeated independently three times with similar results.



**Extended Data Fig. 5 | Effects of Dlp class glypicans on Wingless signalling.**

**a**, GPC4 and GPC6, but not GPC3 and GPC5, driven with *ptc-Gal4* inhibit the high target gene *senseless*. Scale bars, 50  $\mu\text{m}$ . **b**, GPC4 and GPC6, but not GPC3 and GPC5, expressed with *en-Gal4* extend the range of the low target gene *Distal-less* in the posterior compartment. Scale bars, 50  $\mu\text{m}$ . **b'**, *Distal-less* immunoreactivity was quantified in the indicated boxed regions and plotted separately for the anterior and posterior, where the glypicans were overexpressed. **c**, Dlp conditioned medium stabilizes GFP-Wingless in solution. Conditioned medium from S2 cells or S2 cells expressing Dlp<sup>AGPI</sup>-V5 was added to S2 cells expressing GFP-Wingless. Twelve hours later, the medium was collected, concentrated 20-fold and the amount of GFP-Wingless in

solution was determined via western blot. **d**, Wingless solubilized by Dlp<sup>AGPI</sup> is signalling competent. Medium from cells that were mock-transfected, transfected with GFP-Wingless alone, or co-transfected with either V5 tagged Dally<sup>AGPI</sup> or Dlp<sup>AGPI</sup> was collected, concentrated and added to S2R+ cells expressing a luciferase reporter of Wingless signalling. Error bars show standard deviation from the mean.  $n = 4$ , in which  $n$  denotes independent experiments and each independent experiment was performed in triplicate. Asterisk denotes statistical significance, as assessed by an unpaired, two-tailed  $t$ -test ( $P = 0.001$ ). ns, not significant ( $P = 0.128$ ). All experiments were repeated independently three times with similar results.

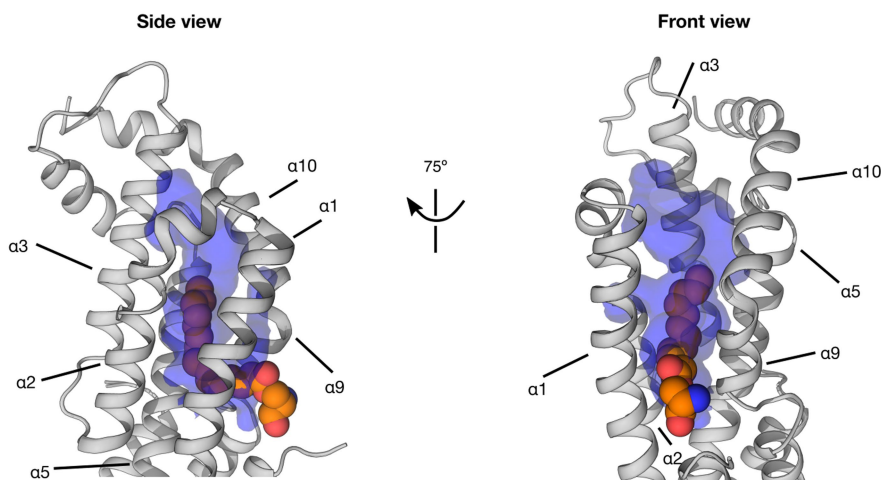


**Extended Data Fig. 6 | Steric clashes prevent Wnt lipid binding to glypican CRD.** **a, b**, CRD architecture for Dlp<sup>core</sup> in complex with palmitoleoylated serine of Wnt peptide. We could confirm that the Dlp<sup>CRD</sup> contains the full set of canonical disulfide bonds. **c–f**, Comparison of the conserved CRD architecture of apo *Drosophila* Dlp<sup>core</sup> (PDB code 3odn) (c), human GPC1 (PDB code 4YWT) (d), mouse Frizzled 8 in complex with palmitoleic moiety from *Xenopus* Wnt8

(PDB code 4F0A) (e) and mouse Frizzled 8 in complex with palmitoleic moiety from human Wnt3 (PDB code 6AHY) (f). Evolutionary conserved disulfides are shown in black and numbered. **g, h**, Superposition of Dlp<sup>core</sup> CRD and mouse Frizzled 8 CRD bound to lipidated Wnt8 (g) or Wnt3 (h), showing that a conserved helix of glypican CRD sterically hinders binding of the Wnt palmitoleate.

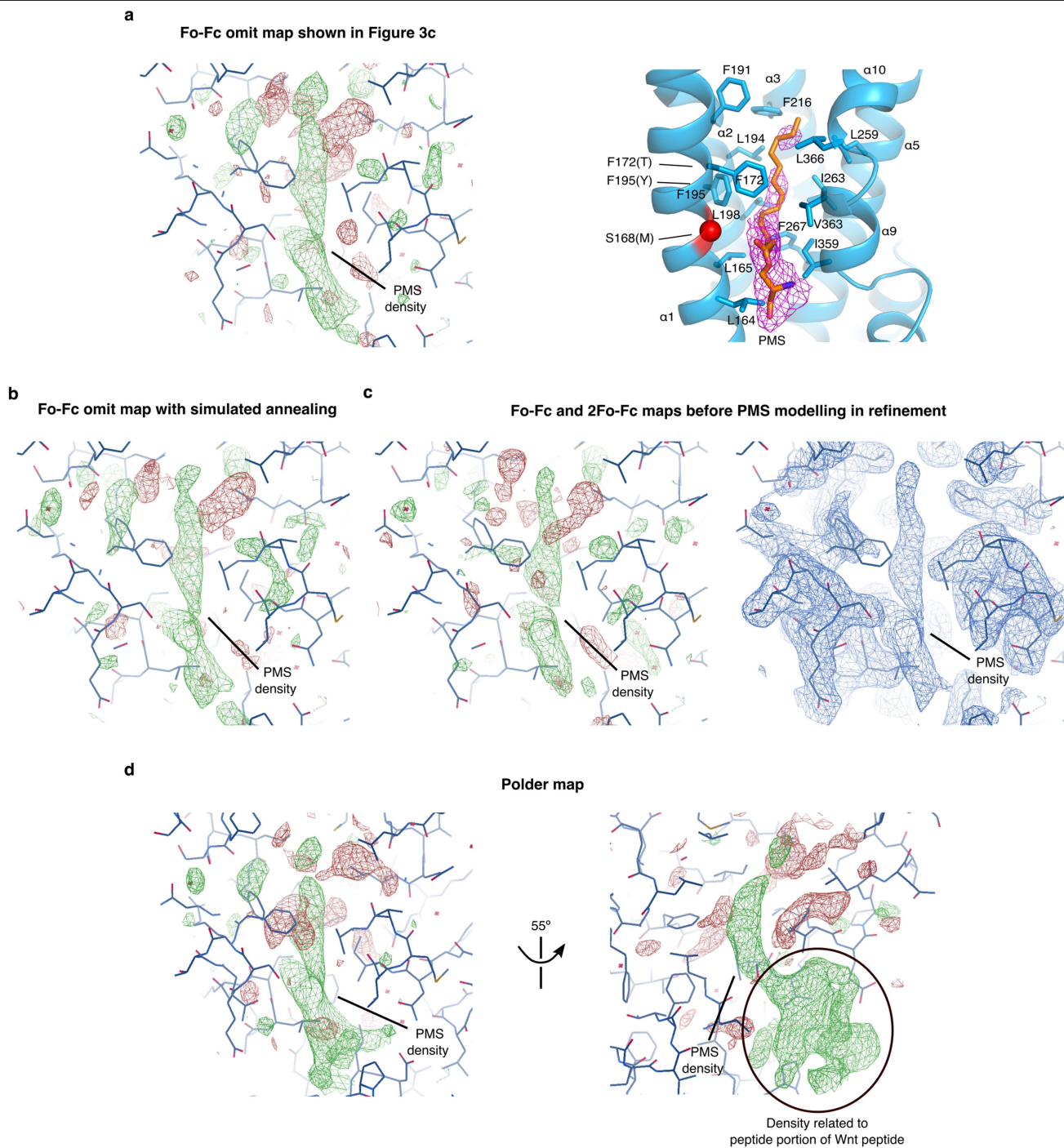


**b**



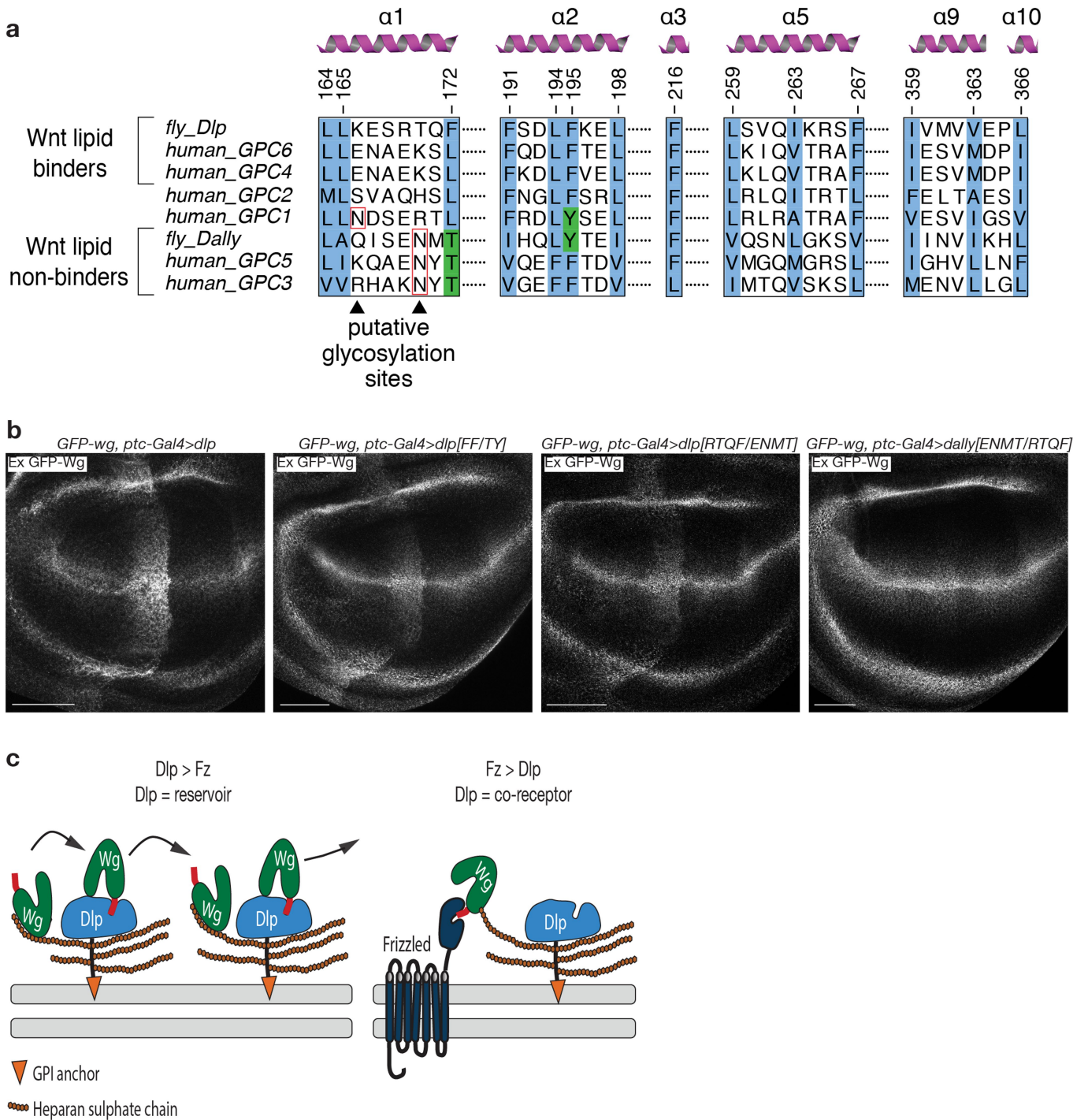
**Extended Data Fig. 7 | Additional structural information on Dlp<sup>core</sup> in complex with human WNT7A peptide.** **a**, Sequence of Dlp<sup>core</sup> construct from the complexed structure annotated with secondary structure elements. To facilitate comparison between the complexed and apo structure, secondary structure nomenclature of the complex reflects that of the previously published apo structure (PDB code 3odn).  $\alpha$  indicates  $\alpha$ -helices,  $\eta$  indicates  $3_{10}$ -helices. **b**, Side and front view of the lipid binding cavity of Dlp<sup>core</sup> in complex

with the Wnt palmitoleoylated peptide, showing the cavity extension beyond the end of the Wnt peptide acyl chain. This additional space likely accommodates the bodipy moiety of bodipy-palmitate for the assays presented in Fig. 4a. The internal volume of the cavity is coloured in blue, with the palmitoleoylated serine from the Wnt peptide represented as spheres in atomic colouring (C: orange, N: blue, O: red).



**Extended Data Fig. 8 | Several types of omit maps show and support the modelling of the electron density in the binding pocket as PMS from the palmitoleoylated Wnt peptide.** **a**, Coot-displayed  $F_o - F_c$  omit map (left) generated from the refined model after removal of PMS, as shown in Fig. 3c. To help orientation and comparison, Fig. 3c is duplicated here, displaying the same map in Pymol (right). The maps are contoured at the same level in the two programs ( $\pm 2.5\sigma$ ). **b**, Coot-displayed  $F_o - F_c$  omit map (contoured at  $\pm 2.5\sigma$ ) generated from the refined model, after removal of PMS, application of simulated annealing and one round of coordinate and B-factor refinement.

**c**, Coot-displayed  $F_o - F_c$  map (left) and  $2F_o - F_c$  map (right) of the last refinement iteration before modelling PMS in the electron density. As PMS was never modelled, these maps are unbiased. The  $F_o - F_c$  map and  $2F_o - F_c$  map are contoured at  $\pm 2.5\sigma$  and  $1\sigma$ , respectively. **d**, Polder map generated from the refined model using phenix.polder<sup>54</sup>. This omit map, the characteristic of which is to enhance weak electron density features in the omit region, shows additional electron density that can be assigned to the peptide portion of the palmitoleoylated peptide, therefore further supporting PMS modelling into the electron density. The map is contoured at  $\pm 2.5\sigma$ .



**Extended Data Fig. 9 | In vivo characterization of Dlp/Dally chimaeras.**

**a**, Multiple sequence alignment of residues forming binding pocket of human and *D. melanogaster* glypicans. Sequences are coloured according to Clustal X colouring scheme (blue, hydrophobics; green, polar). **b**, Extracellular distribution after overexpression of haemagglutinin-tagged Dlp, Dlp(F172T/F195Y; FF/TY), Dlp(R169E/T170N/Q171M/F172T; RTQF/ENMT) or Dally(E149R/N150T/M151Q/T152F; ENMT/RTQF) with *ptc-gal4*. Scale bars, 50  $\mu$ m. **c**, Model illustrating how

Dlp acts both as a reservoir of signalling competent Wnt and as a co-receptor. The weight of these activities depends on the relative abundance of Dlp to Frizzled and on the relative affinities of Dlp and Frizzled for Wnt. Configuration of glypican core and heparan sulfate chains are inspired from the structure of human GPC1<sup>26</sup>. All molecules are drawn approximately to scale. The heparan sulfate chains are presented as orange circles, the glypican stalk regions from which they originate as black lines, and the GPI anchors as orange triangles.

# Article

## Extended Data Table 1 | Data collection and refinement statistics (molecular replacement)

	Dlp-Wnt7a-peptide_complex
PDB ID code	6XTZ
Ligand code	O18
<b>Data collection</b>	
Space group	P2 <sub>1</sub> 2 <sub>1</sub> 2 <sub>1</sub>
Cell dimensions	
<i>a</i> , <i>b</i> , <i>c</i> (Å)	63.7, 77.4, 118.8
$\alpha$ , $\beta$ , $\gamma$ (°)	90, 90, 90
Resolution (Å)	56.14-2.21 (2.25-2.21)*
<i>R</i> <sub>merge</sub>	0.176 (2.026)
<i>I</i> / $\sigma$ <i>I</i>	8 (1.1)
Completeness (%)	100 (100)
Redundancy	13.1 (11.2)
<b>Refinement</b>	
Resolution (Å)	56.14-2.21
No. reflections	30027 (2687)
<i>R</i> <sub>work</sub> / <i>R</i> <sub>free</sub>	0.2267/0.2553
No. atoms	
Protein	3395
Ligand/other	23/46
Water	82
<i>B</i> -factors (Å <sup>2</sup> )	
Protein	62.93
Ligand	78.40
Water	53.29
R.m.s. deviations	
Bond lengths (Å)	0.002
Bond angles (°)	0.38

The diffraction dataset was collected from a single crystal.

\*Values in parentheses are for highest-resolution shell.

## Reporting Summary

Nature Research wishes to improve the reproducibility of the work that we publish. This form provides structure for consistency and transparency in reporting. For further information on Nature Research policies, see [Authors & Referees](#) and the [Editorial Policy Checklist](#).

### Statistics

For all statistical analyses, confirm that the following items are present in the figure legend, table legend, main text, or Methods section.

n/a Confirmed

- The exact sample size ( $n$ ) for each experimental group/condition, given as a discrete number and unit of measurement
- A statement on whether measurements were taken from distinct samples or whether the same sample was measured repeatedly
- The statistical test(s) used AND whether they are one- or two-sided  
*Only common tests should be described solely by name; describe more complex techniques in the Methods section.*
- A description of all covariates tested
- A description of any assumptions or corrections, such as tests of normality and adjustment for multiple comparisons
- A full description of the statistical parameters including central tendency (e.g. means) or other basic estimates (e.g. regression coefficient) AND variation (e.g. standard deviation) or associated estimates of uncertainty (e.g. confidence intervals)
- For null hypothesis testing, the test statistic (e.g.  $F$ ,  $t$ ,  $r$ ) with confidence intervals, effect sizes, degrees of freedom and  $P$  value noted  
*Give  $P$  values as exact values whenever suitable.*
- For Bayesian analysis, information on the choice of priors and Markov chain Monte Carlo settings
- For hierarchical and complex designs, identification of the appropriate level for tests and full reporting of outcomes
- Estimates of effect sizes (e.g. Cohen's  $d$ , Pearson's  $r$ ), indicating how they were calculated

*Our web collection on [statistics for biologists](#) contains articles on many of the points above.*

### Software and code

Policy information about [availability of computer code](#)

Data collection Xia2 (v. 0.5.884-g39f26010-dials-1.14), Dials (v. 1.14.3-g2ab223656-release), Aimless (version 0.7.4) - automated processing of x-ray diffraction data.

Data analysis Inkscape (v. 0.92.2)  
ImageJ (v:2.0.0-rc-69/1.52n)- image analysis  
Illustrator (CC 22.1)- figure preparation  
Licor Image Studio (v. 5.2)- western blot acquisition  
Leica LAS (v.2.7.3.9723)-confocal image acquisition  
Prism (v. 8.0.0 (131))- figure preparation and statistical test calculation  
Phaser (v.2.8.2) - molecular replacement.  
Phenix (v. dev-3386) - refinement, analysis and validation of x-ray diffraction data and atomic models.  
Coot (v. 0.8.9.1) - visualization, building and validation of atomic models.  
Chemdraw (v. 18.1.0.458) - generation of SMILES chemical notation for Wnt peptide.  
Grade Global Phasing web server (v. Release v1.105 Mar 09 2018, <http://grade.globalphasing.org>) - generation of Wnt peptide geometry restraints for crystallographic refinement.  
Molprobrity (v. 4.4) - validation of crystallographic macromolecular models.  
Pymol (v. 2.2.0) - molecular visualization system.  
Jalview (v. 2.10.5) - sequence alignment.  
CASTp web server (v. 3.0, <http://sts.bioe.uic.edu/castp/index.html?1bxw>) - analysis of crystallographic macromolecular models binding pockets.  
FortéBio Octet Data Analysis Software (v. 11.1), SigmaPlot (v.14.0) - Bio-layer interferometry data analysis.

For manuscripts utilizing custom algorithms or software that are central to the research but not yet described in published literature, software must be made available to editors/reviewers. We strongly encourage code deposition in a community repository (e.g. GitHub). See the Nature Research [guidelines for submitting code & software](#) for further information.

## Data

Policy information about [availability of data](#)

All manuscripts must include a [data availability statement](#). This statement should provide the following information, where applicable:

- Accession codes, unique identifiers, or web links for publicly available datasets
- A list of figures that have associated raw data
- A description of any restrictions on data availability

X-ray crystallographic coordinates and structure factor files generated during the current study are available from the RCSB Protein Data Bank (PDB), accession code 6XTZ. Full scans for all western blots are provided in Supplementary Fig. 1. Source Data for Figs. 2&4 and Extended Data Figs. 4&5 are provided with the paper.

## Field-specific reporting

Please select the one below that is the best fit for your research. If you are not sure, read the appropriate sections before making your selection.

Life sciences  Behavioural & social sciences  Ecological, evolutionary & environmental sciences

For a reference copy of the document with all sections, see [nature.com/documents/nr-reporting-summary-flat.pdf](https://www.nature.com/documents/nr-reporting-summary-flat.pdf)

## Life sciences study design

All studies must disclose on these points even when the disclosure is negative.

Sample size	Sample sizes were chosen on the basis of published literature about the methods used and in order to perform statistical analysis.
Data exclusions	Data points were excluded when there was a technical mistake during the experimental procedure.
Replication	Experiments were performed in at least three independent biological replicates and all attempts at replication were successful.
Randomization	Randomization was not used and relevant to this study, since it did not involved an allocation of an intervention or a trial with human or animal participants.
Blinding	Blinding was not used and relevant to this study, since it did not involved an allocation of an intervention or a trial with human or animal participants.

## Reporting for specific materials, systems and methods

We require information from authors about some types of materials, experimental systems and methods used in many studies. Here, indicate whether each material, system or method listed is relevant to your study. If you are not sure if a list item applies to your research, read the appropriate section before selecting a response.

### Materials & experimental systems

n/a	Involved in the study
<input type="checkbox"/>	<input checked="" type="checkbox"/> Antibodies
<input type="checkbox"/>	<input checked="" type="checkbox"/> Eukaryotic cell lines
<input checked="" type="checkbox"/>	<input type="checkbox"/> Palaeontology
<input type="checkbox"/>	<input checked="" type="checkbox"/> Animals and other organisms
<input checked="" type="checkbox"/>	<input type="checkbox"/> Human research participants
<input checked="" type="checkbox"/>	<input type="checkbox"/> Clinical data

### Methods

n/a	Involved in the study
<input checked="" type="checkbox"/>	<input type="checkbox"/> ChIP-seq
<input checked="" type="checkbox"/>	<input type="checkbox"/> Flow cytometry
<input checked="" type="checkbox"/>	<input type="checkbox"/> MRI-based neuroimaging

## Antibodies

Antibodies used	guinea-pig anti-Senseless (gift from H. Bellen), rabbit anti-V5 (Cell Signalling #13202, D3H8Q, Lot.5), mouse anti-V5 (Invitrogen, #R960-25, Lot. 1212316), rabbit anti-GFP (Abcam #ab6556, Lot.GR3271077-1), mouse anti-Wingless (DSHB, 4D4), mouse anti-Hrs (DSHB, 8-2-s), guinea pig anti-ApoL (gift from S. Eaton), rat anti-HA (Roche, 3F10), mouse anti-Ubiquitin (EMD Millipore, FK2, #04-263, Lot 3182603), guinea-pig anti-Distal-less (gift from Richard S. Mann), mouse anti-Beta-Tubulin (DSHB, E7) and rabbit anti-Cherry (Abcam, ab167453, Lot.GR312817-2)
Validation	Previous validations and citations can be found by using the RRID numbers. Guinea-pig anti-Senseless (RRID: AB_2567469), rabbit anti-V5 (RRID:AB_2687461), mouse anti-V5 (RRID:AB_2556564), rabbit anti-GFP (RRID:AB_305564), mouse anti-Wingless (RRID:AB_528512), mouse anti-Hrs (RRID:AB_2722114), guinea pig anti-ApoL (see Panáková D et al., Nature Volume 435, pages58–65 (2005), mouse anti-Ubiquitin RRID:AB_10681625), guinea-pig anti-Distal-less (RRID:AB_2568818), mouse anti-Beta-Tubulin (RRID:AB_528499), rabbit anti-Cherry (RRID:AB_2571870)

## Eukaryotic cell lines

Policy information about [cell lines](#)

Cell line source(s)	HEK293S-GnTI TetR (see article, ref. 35) HEK293T (ATCC CRL-3216) HEK293S-GnTI (ATCC CRL-3022) S2 (DGRC: Stock Number: 6, FlyBase Report: FBtc0000006) S2R+ (DGRC: Stock Number: 150, FlyBase Report: FBtc0000150)
Authentication	Authentication was not performed for this study.
Mycoplasma contamination	The cells tested negative for mycoplasma contamination.
Commonly misidentified lines (See <a href="#">ICLAC</a> register)	The study did not involve any commonly misidentified cell lines.

## Animals and other organisms

Policy information about [studies involving animals](#); [ARRIVE guidelines](#) recommended for reporting animal research

Laboratory animals	Drosophila Melanogaster. Males and Females. Details of lines generated in the course of this study can be found in the methods section. Details of all other lines, Gal4 driver lines and loss of function mutants used in this study, can be found on the public repository flybase.
Wild animals	The study did not involve wild animals.
Field-collected samples	The study did not involve field-collected samples.
Ethics oversight	No ethical approval or guidance required. Invertebrate animals such as Drosophila are not protected by the law or monitored by the Home Office.

Note that full information on the approval of the study protocol must also be provided in the manuscript.